NAVAL POSTGRADUATE SCHOOL
Monterey, California

THESIS

PREDICTABILITY OF JAPAN/EAST SEA (JES) SYSTEM TO UNCERTAIN INITIAL/ LATERAL BOUNDARY CONDITIONS AND SURFACE WINDS

by

Chin-Lung Fang

September 2003

Thesis Advisor:	Peter C. Chu
Second Reader:	Steve Haeger

Approved for public release; distribution is unlimited.

THIS PAGE INTENTIONALLY LEFT BLANK

REPORT DOCUMENTATION PAGE		*Form Approved OMB No. 0704-0188*

Public reporting burden for this collection of information is estimated to average 1 hour per response, including the time for reviewing instruction, searching existing data sources, gathering and maintaining the data needed, and completing and reviewing the collection of information. Send comments regarding this burden estimate or any other aspect of this collection of information, including suggestions for reducing this burden, to Washington headquarters Services, Directorate for Information Operations and Reports, 1215 Jefferson Davis Highway, Suite 1204, Arlington, VA 22202-4302, and to the Office of Management and Budget, Paperwork Reduction Project (0704-0188) Washington DC 20503.

1. AGENCY USE ONLY *(Leave blank)*	2. REPORT DATE September 2003	3. REPORT TYPE AND DATES COVERED Master's Thesis	
4. TITLE AND SUBTITLE: Predictability of Japan/East Sea (JES) System to Uncertain Initial/ Lateral Boundary Conditions and Surface Winds		5. FUNDING NUMBERS	
6. AUTHOR Chin-Lung Fang			
7. PERFORMING ORGANIZATION NAME(S) AND ADDRESS(ES) Naval Postgraduate School Monterey, CA 93943-5000		8. PERFORMING ORGANIZATION REPORT NUMBER	
9. SPONSORING /MONITORING AGENCY NAME(S) AND ADDRESS(ES) NAVOCEANO Stennis Space Center, MS 39522-5001		10. SPONSORING/MONITORING AGENCY REPORT NUMBER	

11. SUPPLEMENTARY NOTES The views expressed in this thesis are those of the author and do not reflect the official policy or position of the Department of Defense or the U.S. Government.

12a. DISTRIBUTION / AVAILABILITY STATEMENT Approved for public release; distribution is unlimited.	12b. DISTRIBUTION CODE

13. ABSTRACT

Numerical ocean modeling usually composes various initial- and boundary-value problems. It integrates hydrodynamic and thermodynamic equations numerically with atmospheric forcing and boundary conditions (lateral and vertical) from initial states of temperature, salinity and velocity. Past observations, historical datasets and climatological datasets of the ocean have contributed greatly to the knowledge of the data fields of initial condition, atmospheric forcing and boundary conditions. Change in either initial or boundary condition leads to a variety of model solutions. It is necessary to specify realistic initial and boundary conditions to achieve better understanding and prediction of the ocean behavior. However, uncertainty often exists in both initial and boundary conditions. Up to now, most studies on ocean predictability have usually been for one particular type of model input uncertainty within the three types of uncertainty (initial conditions, open boundary conditions, atmospheric forcing function). This thesis investigates the response of ocean model to the three types of model input uncertainty simultaneously using Princeton Ocean Model (POM) implemented for the Japan/East Sea (JES).

14. SUBJECT TERMS Initial conditions, wind forcing, lateral boundary transport, POM, JES.			15. NUMBER OF PAGES 95
			16. PRICE CODE
17. SECURITY CLASSIFICATION OF REPORT Unclassified	18. SECURITY CLASSIFICATION OF THIS PAGE Unclassified	19. SECURITY CLASSIFICATION OF ABSTRACT Unclassified	20. LIMITATION OF ABSTRACT UL

NSN 7540-01-280-5500

Standard Form 298 (Rev. 2-89)
Prescribed by ANSI Std. 239-18

i

THIS PAGE INTENTIONALLY LEFT BLANK

PREDICTABILITY OF JAPAN/EAST SEA (JES) SYSTEM TO UNCERTAIN INITIAL/ LATERAL BOUNDARY CONDITIONS AND SURFACE WINDS

Chin-Lung Fang
Lieutenant Commander, Taiwan, R.O.C. Navy
B.S., Chinese Naval Academy, Taiwan, R.O.C., 1992

Submitted in partial fulfillment of the
requirements for the degree of

MASTER OF SCIENCE IN METEOROLOGY AND PHYSICAL OCEANOGRAPHY

from the

**NAVAL POSTGRADUATE SCHOOL
September 2003**

Author: Chin-Lung Fang

Approved by: Peter C. Chu
                 Thesis Advisor

                 Steve Haeger (NAVO)
                 Second Reader

                 Mary Batteen
                 Chairman, Department of Oceanography

THIS PAGE INTENTIONALLY LEFT BLANK

ABSTRACT

Numerical ocean modeling usually composes various initial- and boundary-value problems. It integrates hydrodynamic and thermodynamic equations numerically with atmospheric forcing and boundary conditions (lateral and vertical) from initial states of temperature, salinity and velocity. Past observations, historical datasets and climatological datasets of the ocean have contributed greatly to the knowledge of the data fields of initial condition, atmospheric forcing and boundary conditions. Change in either initial or boundary condition leads to a variety of model solutions. It is necessary to specify realistic initial and boundary conditions to achieve better understanding and prediction of the ocean behavior. However, uncertainty often exists in both initial and boundary conditions. Up to now, most studies on ocean predictability have usually been for one particular type of model input uncertainty within the three types of uncertainty (initial conditions, open boundary conditions, atmospheric forcing function). This thesis investigates the response of ocean model to the three types of model input uncertainty simultaneously using Princeton Ocean Model (POM) implemented for the Japan/East Sea (JES).

THIS PAGE INTENTIONALLY LEFT BLANK

TABLE OF CONTENTS

LIST OF FIGURES

x

LIST OF TABLES

THIS PAGE INTENTIONALLY LEFT BLANK

ACKNOWLEDGMENTS

THIS PAGE INTENTIONALLY LEFT BLANK

I.   INTRODUCTION

Numerical ocean modeling usually composes various initial- and boundary-value problems. It integrates hydrodynamic and thermodynamic equations numerically with atmospheric forcing and boundary conditions (lateral and vertical) from initial states of temperature (T), salinity (S) and velocity. Past observations, historical datasets and climatological datasets of the ocean have contributed greatly to the knowledge of the data fields of initial condition, atmospheric forcing and boundary conditions. Change in either initial or boundary condition leads to a variation of model solutions (Lorenz, 1963; Chu, 1999b). It is necessary to specify realistic initial and boundary conditions to achieve better understanding and prediction of the ocean behavior. However, uncertainty often exists in both initial and boundary conditions.

The first difficult problem in ocean modeling (regional and basin-scale) is that initial velocity field is usually not available due to an insufficient number of velocity observations. A widely used model initialization is the diagnostic mode, which integrates the model from known T, S, such as climatological data (Tc, Sc) and zero velocity fields, while holding Tc and Sc unchanged. After a period (about 30 days) of the diagnostic run, the velocity field (Vc) is established, and Tc, Sc and Vc fields are treated as the initial conditions for numerical prognostic modeling. Recently, Chu and Lan (2003) found that during the diagnostic initialization period, unrealistic heat and salt 'source/sink' terms are generated at each time step.

The second difficult problem in regional ocean modeling is the uncertainty of the open boundary condition (Chu et. al., 1997). At open boundaries where the numerical grid ends, the fluid motion should be unrestricted since ideal open boundaries are transparent to motions. Two approaches, local-type and inverse-type, are available for determining open boundary condition (OBC). The local-type approach determines the OBC from the solution of the governing equations near the boundary. The problem now becomes selecting from a set of ad hoc OBCs. Since any ad hoc OBC will introduce inaccuracies into a numerical solution (Chapman, 1985), it is important to choose the best one from ad hoc OBCs for a particular ocean model. Using a barotropic coastal ocean

model Chapman (1985) evaluated several of the most used ad hoc OBCs (clamped, sponge, radiation) and found that the best OBC consists of a sponge at the outer edge of the model domain with an Orlanski radiation condition (Orlanski, 1976) while determining that the clamped OBC is probably the worst choice. Applying these results to other ocean models needs further investigation. The local approach suffers drawbacks that may restrict its use: no observational data considered and the ill-posedness of the primitive equations model with ad hoc OBC; in other words, it is hard to prove the existence of a unique solution (Bennett, 1992; Oliger and Sundstrom, 1978). To improve the local approach by using observations at open boundaries, Shulman and Lewis (1995) proposed a method for determining OBCs of the shallow water model. Their method is based on the integration of governing equations forward in time and the selection of OBCs via a specific inverse problem that minimizes a measure of difference (energy flux) between the values of observed and predicted variables at open boundaries. Thus, their method helps in selecting proper ad hoc OBC by using observations at the open boundaries.

Without any ad hoc OBC, the inverse-type approach can determine the OBC from the "best" fit between model solutions and interior observations. The most popular scheme for this approach is an adjoint method, which consists of four elements: a set of control parameters or a control vector (e.g., the unknown OBC), a numerical ocean model, a cost function, and an adjoint equation. The cost function is usually defined by the difference between observations and their model counterparts. The adjoint equation is derived from minimizing the cost function with respect to the control parameters. The advantage of using the adjoint method is the well posedness and the use of observational data. Seiler (1993) successfully determines the unknown OBCs for a quasi-geostrophic ocean by using the adjoint method. The disadvantages that may restrict its use are the requirement of large amounts of computer time and memory, problems of stable integration of the adjoint equation, the ocean-model dependency of the adjoint equation, and difficulty in deriving the adjoint equation when the model contains rapidly changing processes, such as ocean mixed layer dynamics. Chu et al. (1997) propose a simplified method that overcomes the disadvantage of the current inverse-type approach. This method can determine OBCs of any ocean model (i.e., a universal method) from interior

2

observations. The essence of the method is to seek the relationship among three vectors: open boundary parameter vector (**B**), observation vector (**O**), and solution vector (**S**). If **B** is given, we can integrate the numerical ocean model and get the solution vector (**S**). If **B** is unknown, the optimization method is used to determine **B** by minimizing the root-mean square difference between **O** and **S**.

The third difficult problem is the uncertainty in the atmospheric forcing function. This is largely due to the lack of meteorological observations over the ocean surface. For example, Chu et al. (1999c) found significant difference in wind forcing over the South China Sea during the lifetime of tropical cyclone Ernie (November 4-18, 1996) between NASA's Scatterometer (NSCAT) and NOAA's National Centers for Environmental Prediction (NCEP) winds. The root-mean-square difference increased from 3.6 m s^{-1} on November 1 to a maximum value of 6.7 m s^{-1} on November 4, 1996, which was the day the boundary current was strongest, fluctuating afterward between 6.7 and 2.7 m s^{-1}. It varied from 50 to 100% of the internal wind variability and equaled the internal wind variability on November 12. Chu et al. (1999c) further investigated the model uncertainty due to the uncertainty of the surface boundary conditions using the Princeton Ocean Model (POM) with 20 km horizontal resolution and 23 sigma levels conforming to a realistic bottom topography during the lifetime of tropical cyclone Ernie (November 4-18, 1996). The uncertainty in surface winds generated uncertainty in currents and thermohaline structure. The root-mean-square difference of currents between NSCAT and NCEP runs decreased with depth, increased with time, and rose to a maximum value of 18 cm s^{-1}, occurring at the surface on November 30. This varied from 47 to 102% of the internal variability of the surface currents. The uncertainty in surface winds generated uncertainty in temperature. The root-mean-square difference of temperature between NSCAT and NCEP runs increased in depth from the surface to a subsurface level (sigma =-0.025) by a maximum value of 0.52°C.

Within the nonlinear dynamics community, three types of sensitivity are commonly discussed: sensitivity to initial conditions, sensitivity to parameters, and sensitivity to boundary conditions. The first type of sensitivity has received a great deal of attention, the second has received a good deal of attention, but the third has received relatively little attention. Recently, Chu (1999b) found that two kinds of predictability

problems exist in the Lorenz system, namely, the model sensitivity to initial (first kind) and boundary (second kind) perturbations. The effect of the boundary error on the model can be represented as a forcing term.

Introducing the same small relative error (10^{-4}) to either the initial or boundary condition, the Lorenz system has a growing period and an oscillation period. During the growing period, the model error increases from 0 to an evident value larger than 1. During the oscillation period, the model error oscillates between two evident values. For the wide range of the parameter space, both the error growing period and the relative error are comparable between the first kind of problem (initial inaccuracy) and the second kind of problem (boundary inaccuracy). This suggests the importance of preparing accurate boundary conditions for numerical prediction. The Lorenz system is a low order (three components) convective model. As a result the following question arises: do the two types of predictability in Lorenz system also exit in realistic regional ocean models? The boundaries in ocean models include upper boundary (atmospheric forcing) and lateral boundary. Ocean model uncertainty caused by the errors in the atmospheric forcing functions, such as surface winds and thermohaline fluxes and/or in the lateral open boundary conditions is the second kind of predictability. In ocean models, the two kinds of uncertainty may occur together. The effect of joint initial/boundary condition errors on the model performance is defined as the third kind of predictability.

Up to now, most studies on ocean predictability have usually been for one particular type of model input uncertainty within the three types of uncertainty (initial conditions, open boundary conditions, atmospheric forcing function). This thesis investigates the three types of model input uncertainty simultaneously using Princeton Ocean Model (POM) for the Japan/East Sea (JES).

It is organized into the following chapters in this thesis. In chapter II, the oceanography of the Japan/East Sea (JES) is described. In Chapter III, the Princeton Ocean Model (POM) is introduced. In Chapter IV, the experimental design is described. In Chapters V, the analysis methods are introduced. In Chapter VI, model errors due to input uncertainty are investigated. Finally, in Chapter VII, the conclusions are presented.

II.   JAPAN/EAST SEA (JES) OCEANOGRAPHY

The Japan Sea, known as the East Sea in Korea, has steep bottom topography (Fig. 1) that makes it a unique semi-enclosed ocean basin overlaid by a pronounced monsoon surface wind. The Japan/East Sea, hereafter referred to as JES, covers an area of 10^6 km^2. It has a maximum depth in excess of 3,700 m, and is isolated from open oceans except for small (narrow and shallow) straits. The JES connects with the North Pacific through the Korea/Tsushima and Tsugaru Straits and with the Okhotsk Sea through the Soya and Tatar Straits. In addition, the JES contains three major basins called the Japan Basin (JB), Ulleung/Tsushima Basin (UTB), and Yamato Basin (YB); it also has a high central plateau called the Yamato Rise (YR). The JES is of great scientific interest as a miniature prototype ocean. Its basin-wide circulation pattern, boundary currents, Subpolar Front (SPF), mesoscale eddy activities and deepwater formation are similar to those in a large ocean.

A.   THE THERMOHALINE STRUCTURE

The thermohaline structure of JES has been studied by many investigators (Gong and Park, 1969; Isoda and Saitoh, 1993; Isoda et al., 1991; Maizuru Mar. Observ., 1997) using limited data sets. For example, after analyzing satellite infrared (IR) images and routine hydrographic survey data (by the Korea Fisheries Research and Development Agency) for the western part of the JES in the winter and the spring 1987, Isoda and Saitoh (1993) found that a small meander of a thermal front originates from the Korean/Tsushima Strait near the Korean coast gradually growing into an isolated warm eddy with a horizontal scale of 100 km. The warm eddy moves slowly northward from spring to summer.

Although the seasonal thermal variability on 150 m depth is weaker than on the surface, SPF still occurs at around 40°N consistently throughout the year, and it is located at almost the same location as at the surface. It divides the water masses with different characteristics. North of the SPF, the temperature is uniformly cold ($1°$–$3°$C) throughout the year. South of the SPF, the temperature changes from $5°$C to $9°$C. The SPF

meandering at 131°E, 134°E, and 138°E forms several mesoscale eddies (Chu et al., 2001a,b). The SPF meandering near Okin Gunto (134° E) in spring was previously reported by Isoda and Saitoh (1993).

With limited data, Miyazaki (1953) found a low salinity layer in the SPF region. Later on Kim and Chung (1984) found very similar property in UTB which they called the JES Intermediate Water (JIW). After analyzing the comprehensive hydrographic data for the whole JES collected by the Japan Meteorological Agency, the Maizuru Marine Observatory, and the Hydrographic Department of the Japan Maritime Safety Agency, Senjyu (1999) demonstrates the existence of a salinity minimum (SMIN) layer (i.e., JIW) between the TWC Water and the JES Proper Water. The southwestern JES west of 132°E is the upstream region of JIW. The lowest salinity and the highest oxygen concentration are found in the 38°-40°N areas west of 132°E. The JIW takes two flow paths: an eastward flow along the SPF and a southward flow parallel with the Korean coast in the region west of 132°E. Analyzing the hydrographic collected from an international program, Circulation Research of the East Asian Marginal Seas (CREAMS), Kim and Kim (1999) discovered the high salinity water with high oxygen in the eastern JB (i.e., north of SPF) naming it the High Salinity Intermediate Water (HSIW).

Recently, Chu et al. (1998; 1999a) reported the seasonal occurrence of JES eddies from the composite analysis of the U.S. National Center for Environmental Prediction's (NCEP) monthly SST fields (1981-1994). For example, they identified a warm center appearing in late spring in the East Korean Bay. Chu et al. (2001a,b) further reported the seasonal variation of the thermohaline structure and inverted circulation from the Navy's unclassified Generalized Digital Environmental Model (GDEM) temperature and salinity data on a 0.5° × 0.5° grid using the P-vector method (Chu, 1995). The GDEM for the JES was built on 136,509 temperature and 52,572 salinity (1930-1997) historical profiles. A three-dimensional estimate of the absolute geostrophic velocity field was obtained from the GDEM temperature and salinity fields using the P-vector method. The climatological mean and seasonal variabilities of the thermohaline structure and the inverted currents, such as the SPF, the mid-level (50 to 200 m) salty tongue, the Tsushima Warm Current (TWC) and its bifurcation, were identified. Using the data collected from Conductivity-Temperature-Depth (CTD) and Acoustic Doppler Current Profilers (ADCP)

measurements in the southwestern JES from March to June 1992, Shin et al. (1995, 1996) found a dipole structure of gyres with an anticyclonic eddy near the Korean coast and a cyclonic eddy in the UTB.

B.   CURRENT SYSTEMS

Most of the nearly homogeneous water in the deep part of the basin is called the Japan Sea Proper Water (Moriyasu, 1972) and is of low temperature and low salinity. Above the Proper Water, the Tsushima Warm Current (TWC), dominating the surface layer, flows in from the East China Sea through the Korea/Tsushima Strait carrying warm water from the south. The Liman Cold Current (LCC) carries cool fresh surface water from the north and northeast (Seung and Kim, 1989; Holloway et al., 1995). The properties of this surface water are generally believed to be determined by the strong wintertime cooling coupled with fresh water input from the Amur River and the melting sea ice in Tatar Strait (Martin and Kawase, 1998). The LCC flows southward along the Russian coast, beginning at a latitude slightly north of Soya Strait, terminating off Vladivostok (Fig.2), and becoming the North Korean Cold Current (NKCC) after reaching the North Korean coast (Yoon, 1982a).

The TWC separates into two branches, which flow through the western and eastern channels of the Korea/Tsushima Strait (Kawabe, 1982a,b; Hase et al., 1999). The flow through the eastern channel closely follows the Japanese Coast; it is called the Nearshore Branch (Yoon, 1982b) or the first branch of TWC (FBTWC) (Hase et al., 1999). The flow through the western channel is called the East Korean Warm Current (EKWC), which closely follows the Korean coast until it separates near 37°N into two sub-branches. The western sub-branch moves northward and forms a cyclonic eddy over UTB off the eastern Korean coast. The eastern sub-branch flows eastward to the western coast of Hokkaido Island, and becomes the second branch of the TWC (SBTWC).

The NKCC meets the EKWC at about 38°N with some seasonal meridional migration. After separation from the coast, the NKCC and the EKWC converge forming a strong front that stretches to the zonal direction across the basin. The NKCC makes a cyclonic recirculation gyre in the north, while most of the EKWC flows out through the

Tsugaru and Soya Straits (Uda, 1934). The formation of NKCC and the separation of EKWC are due to local forcing by wind and buoyancy flux (Seung and Nam, 1992). Large meanders associated with warm and cool eddies develop along the front.

C.   ATMOSPHERIC FORCING

The Asian monsoon strongly affects the thermal structure of the JES. During the winter monsoon season, a very cold northwest wind blows over the JES (Fig. 3a) as a result of the Siberian High Pressure System with a mean surface wind speed between 10 and 15 ms^{-1}. By late April, numerous frontally generated events occur making late April and May highly variable in terms of wind speeds and the amount of clouds. During this period, storms originating in Mongolia may cause strong, warm westerlies (Fig. 3b). By late May and early June, a summer surface atmospheric low-pressure system begins to form over Asia. Initially this low-pressure system is centered north of the Yellow Sea producing westerly winds. In late June, this low begins to migrate to the west setting up the southwest monsoon that dominates the summer months. The winds remain variable through June until the Manchurian Low Pressure System strengthens. Despite the very active weather systems, the mean surface wind speed over the JES in summer (Fig. 3c) is between 3 and 4 m/s, much weaker than in winter (Fig. 3a). By July, however, high pressure (the Bonin High) to the south and the low pressure over Manchuria produce southerly winds carrying warm, moist air over the East China Sea/Yellow Sea. In summer, warm air and strong downward net radiation stabilize the upper layer of the JES causing the surface mixed layer to shoal. October (Fig. 3d) is the beginning of the transition to winter conditions. The southerly winds weaken and the sea surface slope establishes its winter pattern.

(UNIT:m)
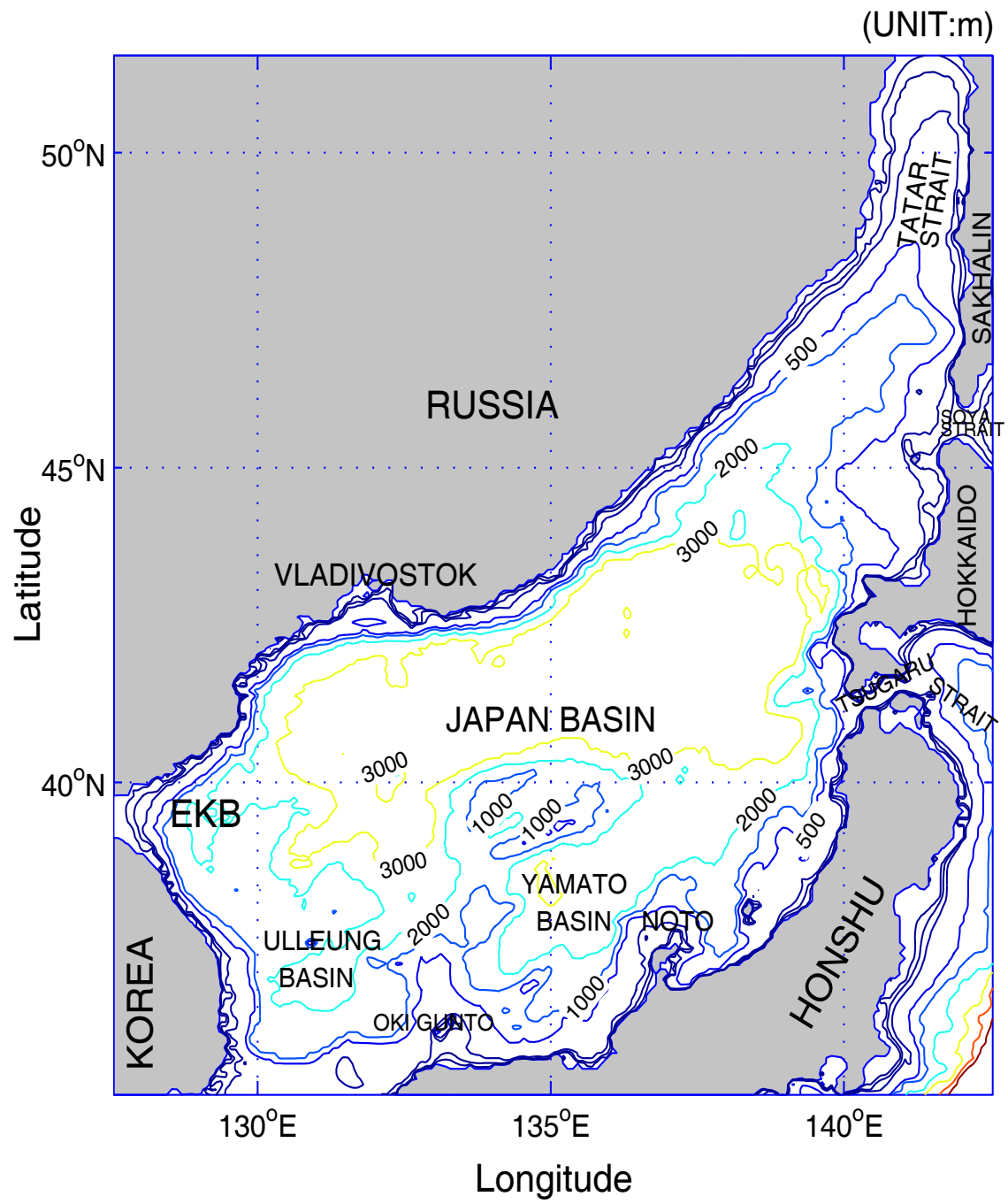
Figure 1. The Japan / East Sea geography and bottom topography.
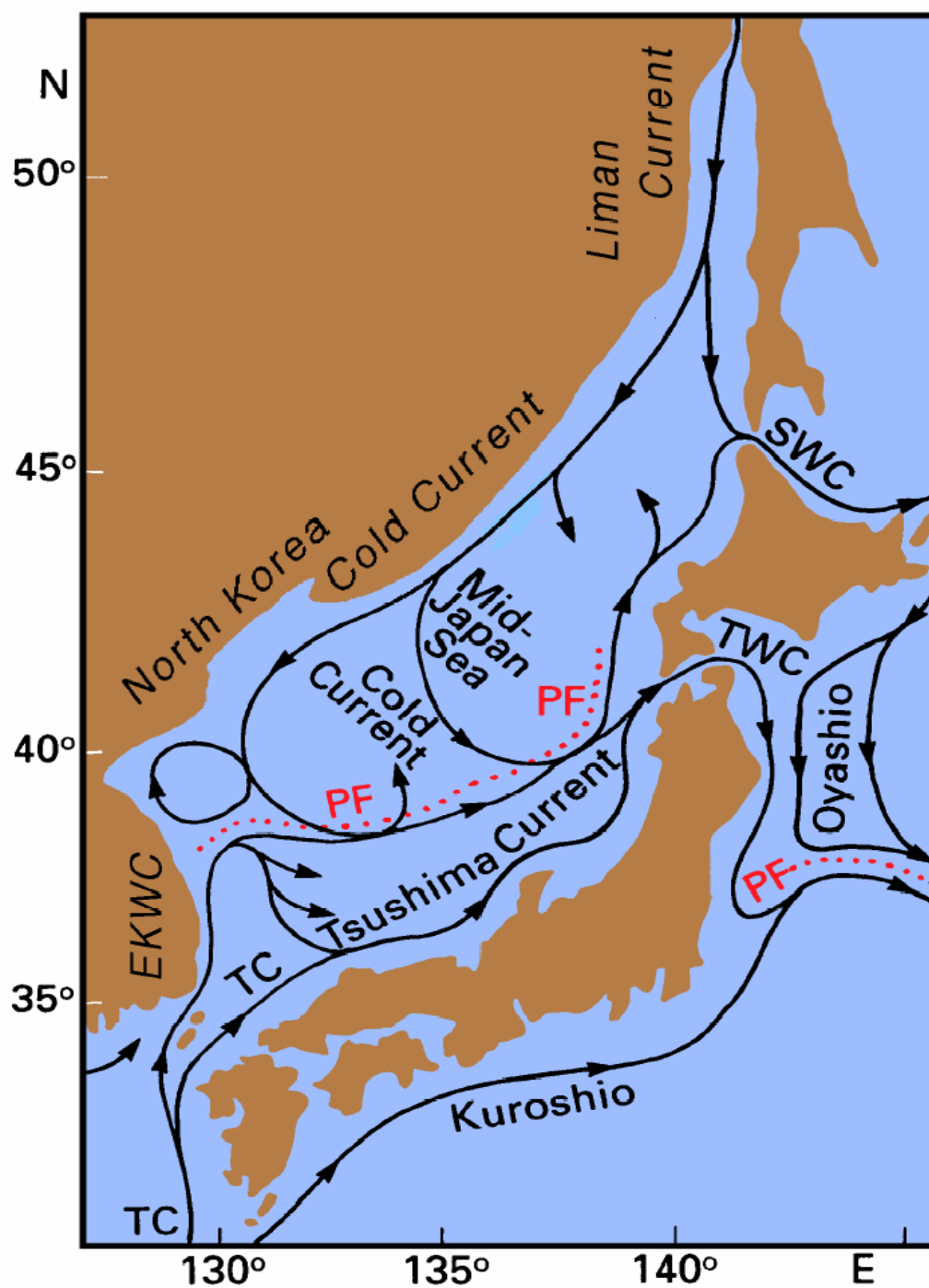
Figure 2.　　Current system in the Japan/East Sea (from Tomczak and Godfrey, 1994).
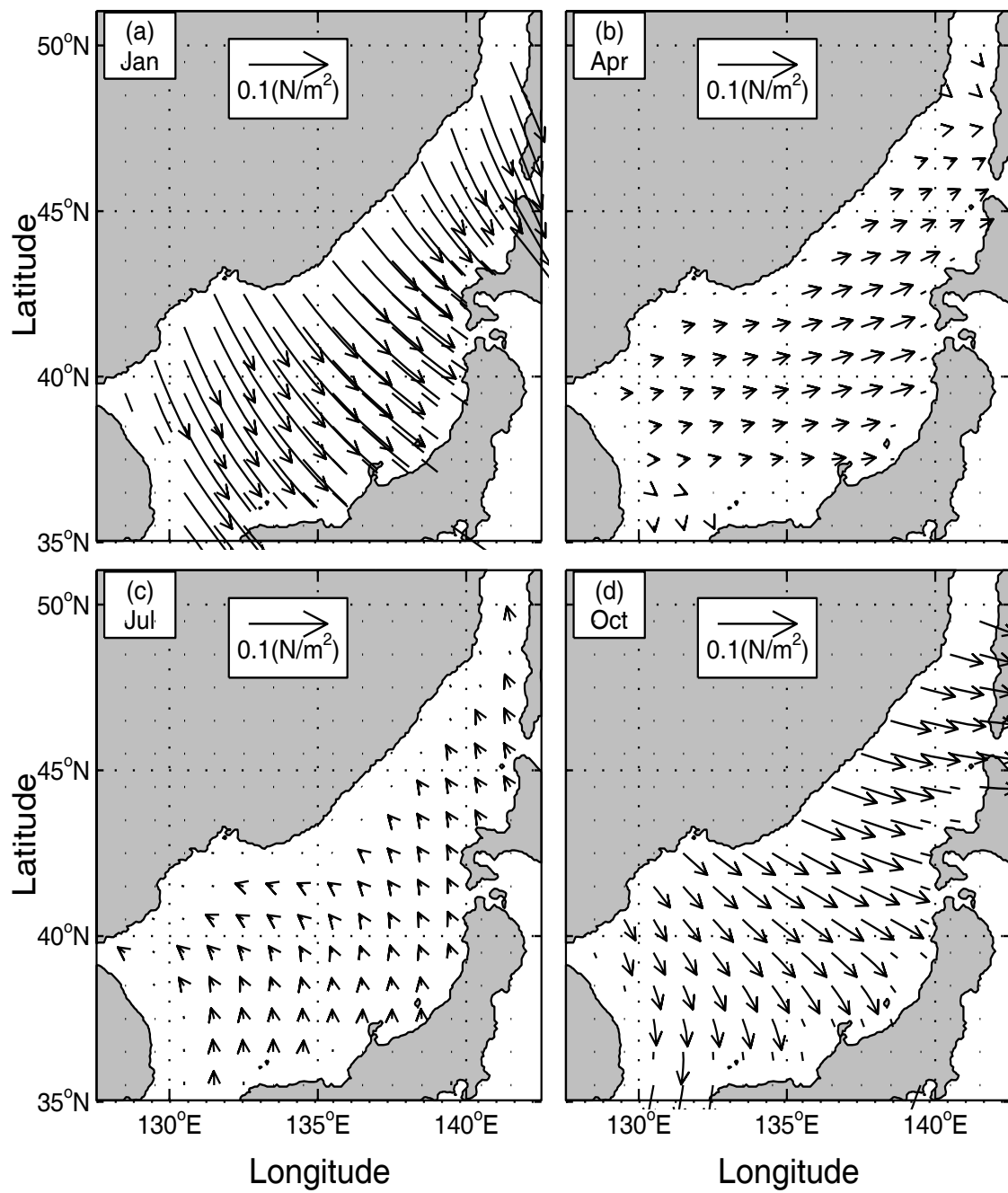
Figure 3.   Climatological wind stress from the COADS data.

THIS PAGE INTENTIONALLY LEFT BLANK

III. THE PRINCETON OCEAN MODEL (POM)

Coastal oceans and semi-enclosed seas are marked by extremely high spatial and temporal variability that challenges the existing predictive capabilities of numerical simulations. The Princeton Ocean Model (POM) is a time-dependent, primitive equation circulation model rendered on a three-dimensional grid that includes realistic topography and a free surface (Blumberg and Mellor, 1987).

In this study, the model contains $91 \times 100 \times 23$ fixed grid points. The horizontal spacing is 10′ latitude and longitude (approximately 11.54 to 15.18 km in the zonal direction and 18.53 km in the meridional direction) with 23 sigma levels in vertical coordinate. The model domain extends from 35.0°N to 51.5°N and from 127.0°E to 142.0°E. The bottom topography (Fig. 1) is obtained from the Naval Oceanographic Office's Digital Bathymetry Data Base 5′ × 5′ resolution (DBDB5). The horizontal friction and mixing are modeled using the Smagorinsky (1963) form with the coefficient chosen to be 0.2 for this application. The bottom stress τ_b is assumed to follow a quadratic law:

$$\tau_b = \rho_o C_D |V_b| V_b \tag{1}$$

where $\rho_0 (= 1025 \text{ kg/m}^3)$ is the characteristic density of the sea water, V_b is the horizontal component of the bottom velocity, and C_D is the drag coefficient specified as 0.0025 (Blumberg and Mellor, 1987). This coefficient is similar to the value (0.002) as used by Hogan and Hurlburt (2000a,b). The significant attributes of the model are as follows:

A. SIGMA COORDINATE

It is a sigma coordinate model in which the vertical coordinate is scaled on the water column depth. The sigma coordinate equations are based on the following transformation:

$$x^* = x, \; y^* = y, \; \sigma = \frac{z - \eta}{H + \eta}, \; t^* = t \tag{2}$$

where x,y,z are the conventional cartesian coordinates; $D \equiv H + \eta$ where $H(x, y)$ is the bottom topography and $\eta(x, y, t)$ is the surface elevation. Thus, σ ranges from $\sigma = 0$ at $z = \eta$ to $\sigma = -1$ at $z = -H$. The sigma coordinate system is necessary in dealing with significant topographical variability, such as that encountered over continental shelf breaks and slopes. Together with the turbulence sub-model, the model produces realistic bottom boundary layers, which are important in coastal waters (Blumberg and Mellor, 1987).

B.   SURFACE FORCING FUNCTIONS

The atmospheric forcing for the JES application of POM includes mechanical and thermohaline forcing. The wind forcing is depicted by

$$\rho_0 K_M \left(\frac{\partial u}{\partial z}, \frac{\partial v}{\partial z} \right)_{z=0} = (\tau_{0x}, \tau_{0y}) \tag{3}$$

where K_M is the vertical mixing coefficient for momentum, (u, v) and (τ_{0x}, τ_{0y}) are the two components of the water velocity and wind stress vectors, respectively. The wind stress at each time step is interpolated from monthly mean climatological wind stress from Comprehensive Ocean-Atmosphere Date Set (COADS 1945-1989), with a resolution of $1° \times 1°$. The COADS wind stress was interpolated into the model grid with a resolution of $10'$.

Surface thermal forcing is depicted by

$$K_H \frac{\partial \theta}{\partial z} = \alpha_1 \left(\frac{Q_H}{\rho C_p} \right) + \alpha_2 C (\theta_{OBS} - \theta) \tag{4}$$

$$K_S \frac{\partial S}{\partial z} = -\alpha_1 FS + \alpha_2 C (S_{OBS} - S) \tag{5}$$

where K_H and K_S are the vertical mixing coefficients for heat and salt, (θ, S) and (θ_{OBS}, S_{OBS}) are the modeled and observed potential temperature and salinity, and c_p is the specific heat. The relaxation coefficient C is the reciprocal of the restoring time period for a unit volume of water. The parameters (α_1, α_2) are (0, 1) switches: $\alpha_1 = 1, \alpha_2 = 0$, would specify only flux forcing is applied. Flux forcing is used in this study.

14

C. LATERAL BOUNDARY FORCING

Boundary conditions for closed lateral boundaries, i.e., the modeled ocean bordered by land, were defined using a free-slip condition for velocity and a zero gradient condition for temperature and salinity. Thus, no advective or diffusive heat, salt or velocity fluxes occur through these boundaries. At open boundaries, the numerical grid terminates, but the fluid motion is unrestricted. Uncertainty at open boundaries makes marginal sea modeling difficult.

Month	Feb.	Apr.	Jun.	Aug.	Oct.	Dec.
Tatar strait (inflow)	*0.05*	*0.05*	*0.05*	*0.05*	*0.05*	*0.05*
Soya strait (outflow)	*-0.1*	*-0.1*	*-0.4*	*-0.6*	*-0.7*	*-0.4*
Tsugaru strait (outflow)	*-0.25*	*-0.35*	*-0.85*	*-1.45*	*-1.55*	*-1.05*
Tsushima strait (inflow)	*0.3*	*0.4*	*1.2*	*2.0*	*2.2*	*1.4*

Table 1   The bi-monthly variation of volume transport (unit: Sv, 1 Sv = 10^6 m^3 s^{-1}).

The bi-monthly volume transports through open boundaries specified from historical data are listed in Table 1. Positive (negative) values are referred to inflow (outflow). Warm water enters the JES through the Korea/Tsushima Strait with the TWC from the East China Sea and exits the JES through the Tsugaru and Soya straits. There is not much information about the volume transport through the Tatar Strait (Martin and Kawase, 1998), which was taken as 0.05 Sv in this study. A recent estimate of the monthly mean volume transport, reported by Yi (1966), through the Korea/Tsushima Strait with the annual average of 1.3 Sv, a maximum of 2.2 Sv in October, and a minimum of 0.3 Sv in February. Bang et al. (1996) used the maximum inflow transport of about 3.5 Sv in August and the minimum of 1.6 Sv in February. In contrast to Yi, Kim and Yoon (1996) used the mean value of 2.2 Sv with +/- 0.35 Sv with the maximum in mid-September and the minimum in mid-March. The total inflow transport through Korea/Tsushima Straits should be the same as the total outflow transport through the

Tsugaru and Soya Straits. We assume that 75% (80% in Bang et al., 1996) of the total inflow transport should flow out of the JES through the Tsugaru Strait, and 25% (20% in Bang et al., 1996) through the Soya Strait. This ratio is adopted from the maximum volume transport through the Tsugaru Strait estimated by Toba et al. (1982), and through the Soya Strait estimated by Preller and Hogan (1998).

D.   MODE SPLITTING

For computational efficiency, the mode splitting technique (Blumberg and Mellor, 1987) is applied with a barotropic time step of 25 seconds, based on the Courant-Friederichs-Levy computational stability (CFL) condition and the external wave speed; and a baroclinic time step of 900 seconds, based on the CFL condition and the internal wave speed.

E.   TWO-STAGE INITILIZATION

1.   The Pre-Simulation Stage

The model was integrated by using two-step initialization. During the first step (restoring run), POM is integrated for two years from zero velocity and climatological temperature and salinity fields (Levitus, 1982) with the climatological monthly mean surface wind stress from the COADS data and restoring-type surface thermohaline forcing ($\alpha_1 = 0$, $\alpha_2 = 1$) which is relaxed to surface monthly mean values.

2.   The Simulation Stage

The final states of the first step (restoring run) are taken as initial conditions for the second step (simulation run). During the simulation run, POM is integrated again for one and half years starting from Julian Day (JD)-1 to JD-180 of the second year with monthly mean surface wind stress, net heat flux, and fresh-water flux ($\alpha_1 = 1$, $\alpha_2 = 0$) from the COADS data. The atmospheric forcing data are temporally interpolated into daily data. The final states of the simulation stage,

$$\mathbf{V}_0 = \mathbf{V}_{JD180}, \quad T_0 = T_{JD180}, \quad S_0 = S_{JD180}, \tag{6}$$

are taken as standard initial conditions for the numerical experiments.

IV.   THE EXPERIMENTAL DESIGN

Uncertainty in the initial/boundary conditions, and atmospheric forcing leads to the uncertainty in model output. The main objective of this study is to investigate the response of a ocean model to uncertain input data using POM implemented for JES. Twelve experiments are conducted with one control run and eleven sensitivity runs (Table 2).

Experiment	Property	Description
0	Control run	See section A
1		
2	Uncertain velocity initialization processes	See section B
3		
4		
5	Uncertain wind stress	See section C
6		
7	Uncertain lateral boundary transport	See section D
8		
9		
10	Combination of uncertainty	See section E
11		

Table 2   Summary of experimental design.

A.   THE CONTROL RUN

The control run is to integrate POM-JES from the standard initial conditions (6) for 180 days (to JD-360) with the lateral transport shown in Table 1 (unperturbed) and the daily surface wind stress, net heat flux, and fresh-water flux ($\alpha_1 = 1$, $\alpha_2 = 0$) interpolated from the COADS monthly mean data (unperturbed).   The simulated temperature and salinity fields and circulation pattern are consistent with observational studies (Chu et al. 2001a).

B.   UNCERTAIN INITIAL CONDITIONS

As mentioned before, initializing the velocity field with the diagnostic mode (called the diagnostic initialization) contains large uncertainty with the possibility of generating extremely strong thermohaline source/sink terms (Chu and Lan, 2003). Four experiments are designed to investigate the model uncertainty to uncertain initial velocity conditions.

Run-1 does not use the velocity initialization. The POM-JES prognostic mode is integrated from

$$\mathbf{V}_0 = 0, \quad T_0 = T_{JD180}, \quad S_0 = S_{JD180}, \tag{7}$$

with the same atmospheric and lateral boundary forcing as Run-0 for 180 days. Model difference between Run-0 and Run-1 is the uncertainty caused by the zero initial velocity fields.

Run-2, Run-3, and Run-4 are designed to investigate the uncertainty of the diagnostic initialization. The POM-JES diagnostic mode is integrated from (7) (T_{JD180}, S_{JD180} unchanged) for 30 days, 60 days, and 90 days to get $\mathbf{V}_{30D}^{(Diag)}$, $\mathbf{V}_{60D}^{(Diag)}$, and $\mathbf{V}_{90D}^{(Diag)}$. The POM-JES prognostic mode is integrated with the same atmospheric and lateral boundary forcing as Run-0 for 180 days from

$$\mathbf{V}_0 = \mathbf{V}_{30D}^{(Diag)}, \quad T_0 = T_{JD180}, \quad S_0 = S_{JD180}, \tag{8}$$

in Run-2; from

$$\mathbf{V}_0 = \mathbf{V}_{60D}^{(Diag)}, \quad T_0 = T_{JD180}, \quad S_0 = S_{JD180}, \tag{9}$$

in Run-3; and from

$$\mathbf{V}_0 = \mathbf{V}_{90D}^{(Diag)}, \quad T_0 = T_{JD180}, \quad S_0 = S_{JD180}, \tag{10}$$

in Run-4 (Table 3).

Experiment	Initial Conditions	Wind Forcing	Lateral Boundary Conditions
1	$\mathbf{V}_0 = 0$, $T_0 = T_{JD180}$, $S_0 = S_{JD180}$	Same as Run-0	Same as Run-0
2	$\mathbf{V}_0 = \mathbf{V}_{30D}^{(Diag)}$, $T_0 = T_{JD180}$, $S_0 = S_{JD180}$	Same as Run-0	Same as Run-0
3	$\mathbf{V}_0 = \mathbf{V}_{60D}^{(Diag)}$, $T_0 = T_{JD180}$, $S_0 = S_{JD180}$	Same as Run-0	Same as Run-0
4	$\mathbf{V}_0 = \mathbf{V}_{90D}^{(Diag)}$, $T_0 = T_{JD180}$, $S_0 = S_{JD180}$	Same as Run-0	Same as Run-0

Table 3   Experiments for uncertain initial conditions.

C.   UNCERTAIN WIND FORCING

Two experiments are conducted to investigate the effect of wind uncertainty. Everything remains the same as Run-0 except the surface winds where a Gaussian-type random variable added to each surface grid point with zero mean and noise intensity of 0.5 m s^{-1} for Run-5 and 1 m s^{-1} for Run-6, respectively (Table 4).

Experiment	Initial Conditions	Wind Forcing	Lateral Boundary Conditions
5	Same as Run-0	Adding Gaussian random noise with zero mean and 0.5 m/s noise intensity	Same as Run-0
6	Same as Run-0	Adding Gaussian random noise with zero mean and 1.0 m/s noise intensity	Same as Run-0

Table 4   Experiments for uncertain wind forcing.

D.   UNCERTAIN LATERAL TRANSPORT

Two experiments are conducted to investigate the effect of lateral transport uncertainty. Everything keeps the same as Run-0 except the lateral boundary transport where a Gaussian-type random variable is added to each lateral boundary grid point with the zero mean and noise intensity being 5% and 10% of the transport (control run) for Run-7 and Run-8, respectively (Table 5).

Experiment	Initial Conditions	Wind Forcing	Lateral Boundary Conditions
7	Same as Run-0	Same as Run-0	Adding Gaussian random noise with the zero mean and noise intensity being 5% of the transport (control run)
8	Same as Run-0	Same as Run-0	Adding Gaussian random noise with the zero mean and noise intensity being 10% of the transport (control run)

Table 5   Experiments for uncertain lateral transport.

E.   COMBINED UNCERTAINTY

Three experiments are conducted to investigate the effect of combined uncertainty. Initial conditions remain the same as Run-2. For Run-9, the surface wind and the lateral boundary transport are the same as Run-6 and Run-0, respectively. For Run-10, the surface wind and the lateral boundary transport are the same as Run-0 and Run-8, respectively. For Run-11, the surface wind and the lateral boundary transport are the same as Run-6 and Run-8, respectively (Table 6).

Experiment	Initial conditions	Wind forcing	Lateral Boundary Conditions
9	Same as Run-2	Same as Run-6	Same as Run-0
10	Same as Run-2	Same as Run-0	Same as Run-8
11	Same as Run-2	Same as Run-6	Same as Run-8

Table 6   Experiments for combined uncertainty.

THIS PAGE INTENTIONALLY LEFT BLANK

V. STATISTICAL ERROR ANALYSIS

A. THE MODEL ERROR

The difference between the variable ψ of control run and each experimental run,

$$\Delta\psi(x,y,z,t) \; = \; \psi_c(x,y,z,t) \; - \; \psi_e(x,y,z,t) \tag{11}$$

represents the model error. Here ψ_c and ψ_e are the variables (u or v components of the horizontal velocity $\mathbf{V}$) from control run and each experimental run, respectively. This model error is used to measure the strength of the effect on each experimental run. We may take the vertically averaging value and probability histogram of $\Delta\psi$ as the error distribution.

B. THE ROOT MEAN SQUARE ERROR

The Root Mean Square Error (RMSE) of the horizontal velocity ($\mathbf{V}$) fields between the control run and each experimental run was computed as

$$RMSE(z,t)_{for\ \mathbf{V}} = \sqrt{\frac{1}{My \times Mx} \sum_{j=1}^{My} \sum_{i=1}^{Mx} \left[\Delta\psi_u(x_i, y_j, z, t)^2 + \Delta\psi_v(x_i, y_j, z, t)^2 \right]} \tag{12}$$

where M_x and M_y are the number of grid points along the east-west direction and the north-south direction for the JES, respectively.

C. THE RELATIVE ROOT MEAN SQUARE ERROR

The Relative Root Mean Square Error (RRMSE) of the horizontal velocity ($\mathbf{V}$) fields between the control run and each experimental run were also computed as

$$RRMSE(z,t)_{for\ \mathbf{v}} = \frac{\sqrt{\sum_{j=1}^{M_y}\sum_{i=1}^{M_x}\left[\Delta\psi_u(x_i,y_j,z,t)^2 + \Delta\psi_v(x_i,y_j,z,t)^2\right]}}{\sqrt{\sum_{j=1}^{M_y}\sum_{i=1}^{M_x}\left[\psi c_u(x_i,y_j,z,t)^2 + \psi c_v(x_i,y_j,z,t)^2\right]}} \tag{13}$$

where M_x and M_y are the number of grid points along the east-west direction and the north-south direction for the JES, respectively.

VI.   MODEL ERRORS DUE TO INPUT UNCERTAINTY

A.   INITIAL CONDITIONS

1.   The Model Error

Based on equation (11) derived in Chapter V, the model error was calculated. For each experimental run (Run 1 to 4), the u and v components of the horizontal velocity (**V**) fields at each grid point were subtracted from those of the control run (Run 0). These errors were used to measure the strength of the effect of various velocity initialization processes used by these four experimental runs.

a.   The Horizontal Distribution

After the model error was calculated for each horizontal grid point, the errors for all the 22 sigma levels were combined vertically for each field on the 5th day (day-185) and the 180th day (day-360) after the day of model integration (day-180). Four plots contained the horizontal distribution of these vertically mean model errors for each specific field (u and v) between the control run and four experimental runs made on the 5th day and the 180th day. The values of max, min, mean and standard deviation were also determined for each plot. These plots are shown in Figure 4 to 7.

As seen in Figure 4, for model errors of u components in the horizontal velocity (**V**) fields on the 5th day, numerous small- to meso-scale patterns of negative and positive model errors are well-mixed and distributed over most of the areas of JES. Near the East Japan Basin, some strong negative and positive patterns are present in Run 2 to 4. At this location, both the maximum negative and positive model errors occur in Run 4 with a value of -0.08 m/s and 0.07 m/s, respectively. Some isolated strong negative and positive model errors are also present near the Ulleung Basin in Run 1 with a value of -0.09 m/s and 0.09 m/s, respectively. These features are similar for the model errors of v components in the horizontal velocity (**V**) fields on the 5th day in Figure 6. Near the East Japan Basin, both the maximum negative and positive model errors occur in Run 4 with a value of -0.13 m/s and 0.13 m/s, respectively. Near the Ulleung Basin, some isolated

strong negative and positive model errors are also present in Run 1 with a value of -0.08 m/s and 0.1 m/s, respectively.

As seen in Figure 5, model errors of u components in the horizontal velocity (**V**) fields on the 180th day reveal several small- to meso-scale patterns concentrated near the Japan Basin on each plot. Near the East Japan Basin, some strong negative and positive patterns are present for all the experimental runs. At this location, the maximum negative model error occurs in Run 2 with a value of -0.05 m/s, which indicates an overestimation in model prediction. On the other hand, the maximum positive model error reached 0.03 $^{\circ}$C in Run 2, which indicates an underestimation in model prediction. These features are similar for the model errors of v components in the horizontal velocity (**V**) fields on the 180th day in Figure 7, with a maximum negative and positive value of -0.07 m/s and 0.05 m/s (Run 2), respectively. As observed, the model errors are present mostly near the Japan Basin. This could be associated with the nearby Polar Front (PF) where two current systems (NKCC and TWC) converge. In general, the model errors of u and v components in the horizontal velocity (**V**) fields are more significant on the 5th day than those on the 180th day. In addition, not much difference exist among the model error distributions for all four experimental runs on both days indicating that the difference among the model errors of these four experimental runs is not significant.

b.   *The Histogram*

The model error, calculated by equation (11), could also be presented in the form of a histogram to evaluate the model error distribution. Four histogram plots contained the model errors in each specific field (u and v) between the control run and four experimental runs made on the 5th day and the 180th day. The values of the number of the total samples, samples greater than zero, samples less than zero and standard deviation were also determined for each plot. These plots are shown in Figure 8 to 9.

In Figure 8, the histogram of model errors of u components in the horizontal velocity on both the 5th day and 180th day reveals a Gaussian-type distribution on each plot. The values of standard deviation (STD) are decreasing with integration

time. For the 5th day, the maximum and minimum values of standard deviation occur in Run 1 and Run 2 with a value of 0.023 m/s and 0.021 m/s, respectively. For the 180th day, the maximum and minimum values of standard deviation occur in Run 1 and Run 3 with a much smaller value of 0.008 m/s and 0.007 m/s, respectively. These features are similar for the histogram of model errors of v components in the horizontal velocity on both the 5th day and 180th day in Figure 9. For the 5th day, the maximum and minimum values of standard deviation occur in Run 4 and Run 2 with a value of 0.025 m/s and 0.023 m/s, respectively. For the 180th day, the maximum and minimum values of standard deviation are occurred in Run 1 and Run 4 with a value of 0.009 m/s and 0.008 m/s, respectively. In general, obvious differences exist between these two days (the model errors are decreasing with time), but the differences among these four experimental runs are still not significant.

Figure 4.   Vertically averaged model error of (a) Run 0 – Run 1, (b) Run 0 – Run 2, (c) Run 0 – Run 3 and (d) Run 0 – Run 4 for u component of velocity field on the 5th day after the model integration.
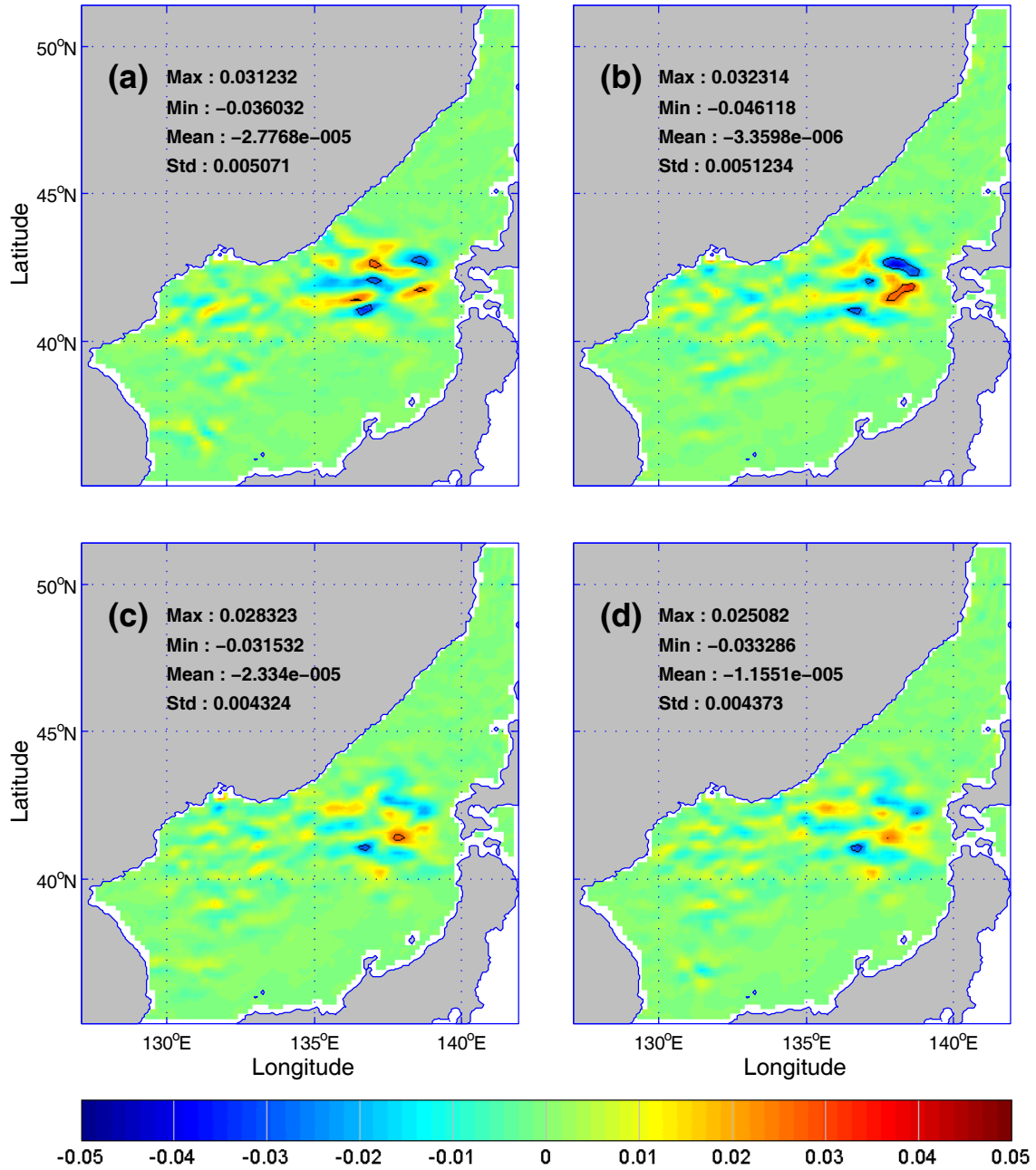
Figure 5.   Vertically averaged model error of (a) Run 0 – Run 1, (b) Run 0 – Run 2, (c) Run 0 – Run 3 and (d) Run 0 – Run 4 for u component of velocity field on the 180th day after the model integration.
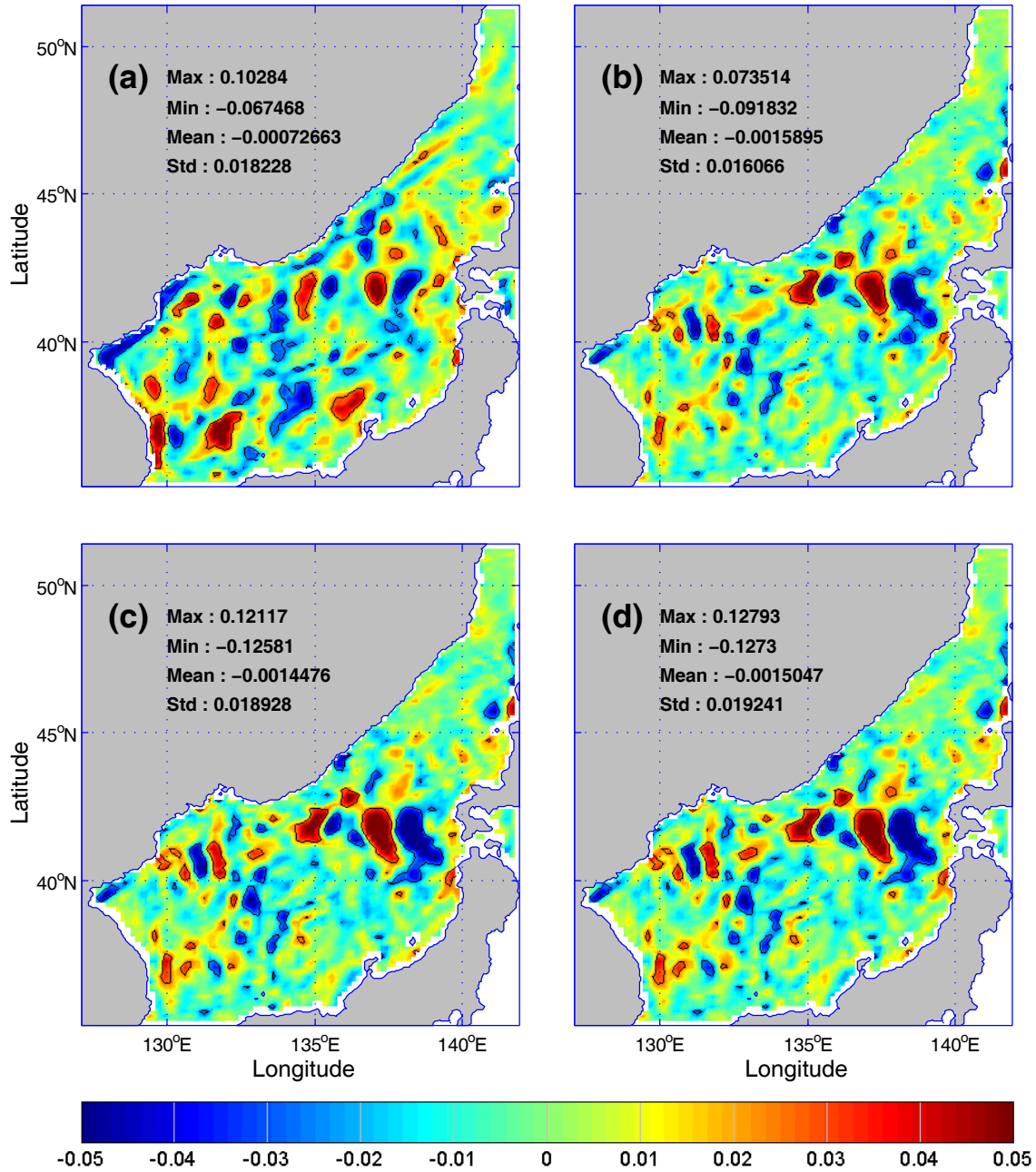
Figure 6.   Vertically averaged model error of (a) Run 0 – Run 1, (b) Run 0 – Run 2, (c) Run 0 – Run 3 and (d) Run 0 – Run 4 for v component of velocity field on the 5th day after the model integration.
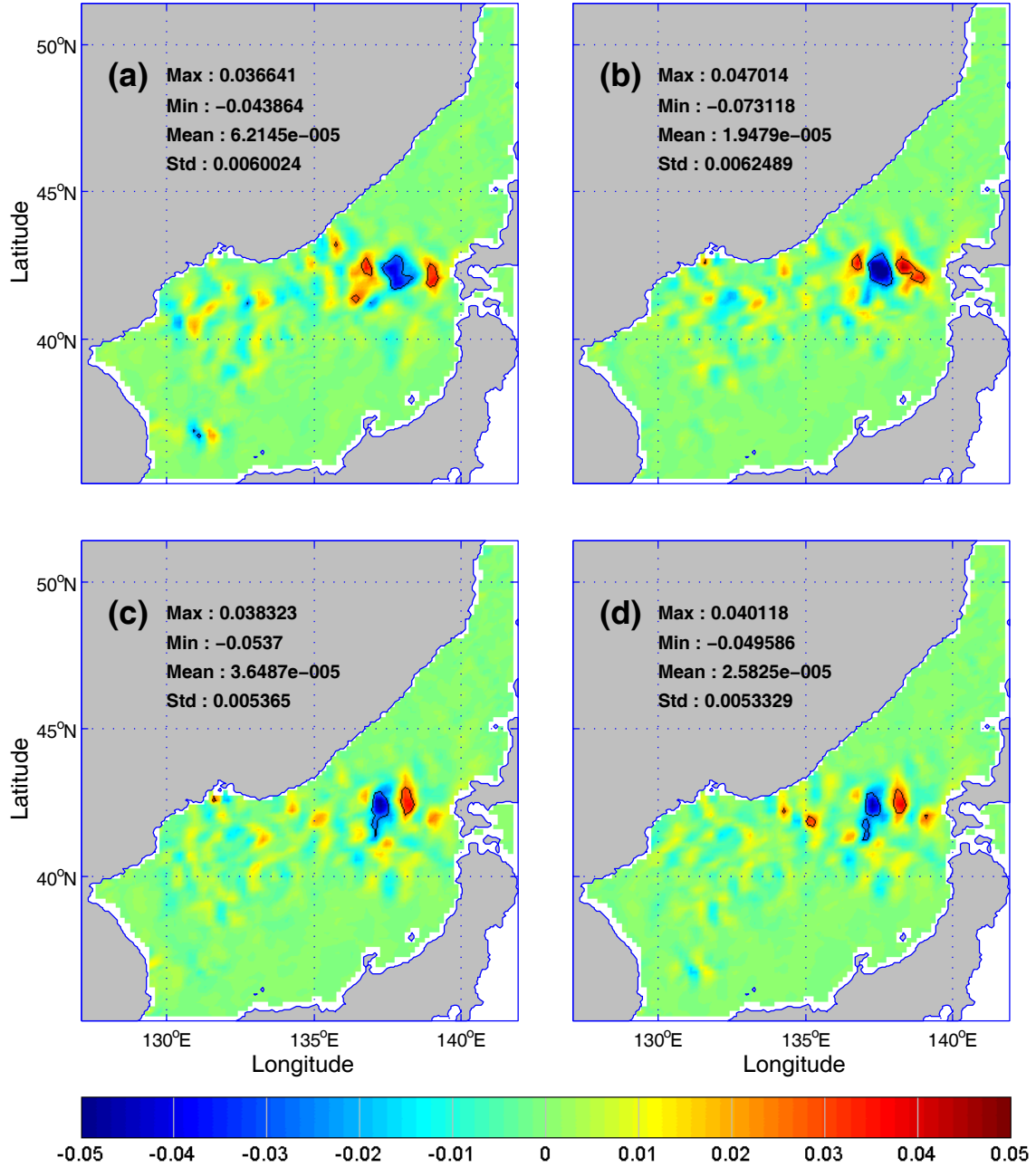
Figure 7.   Vertically averaged model error of (a) Run 0 – Run 1, (b) Run 0 – Run 2, (c) Run 0 – Run 3 and (d) Run 0 – Run 4 for v component of velocity field on the 180th day after the model integration.
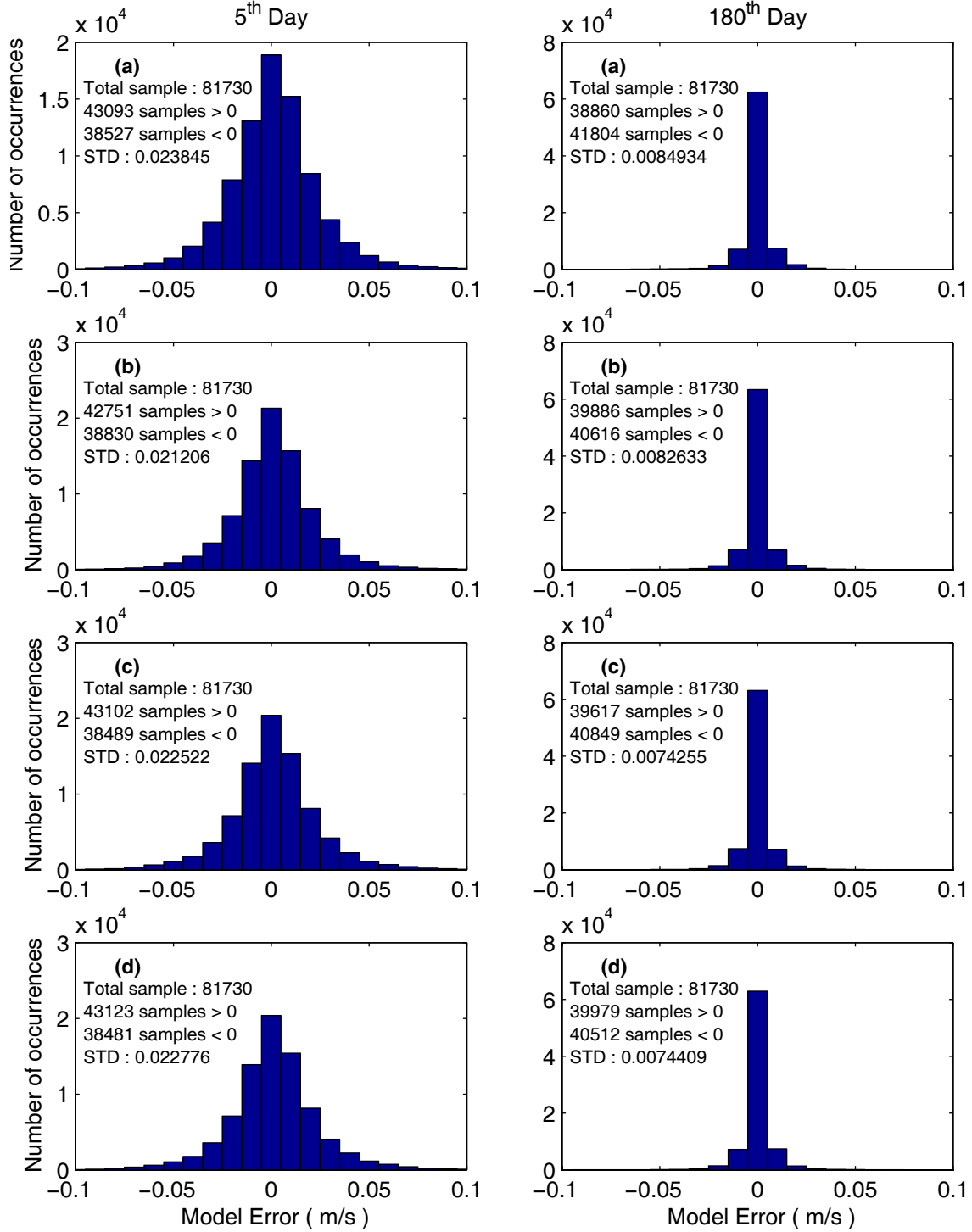
Figure 8.   Histogram of (a) Run 0 – Run 1, (b) Run 0 – Run 2, (c) Run 0 – Run 3 and (d) Run 0 – Run 4 for u component of velocity field on both the 5th and 180th day after the model integration.
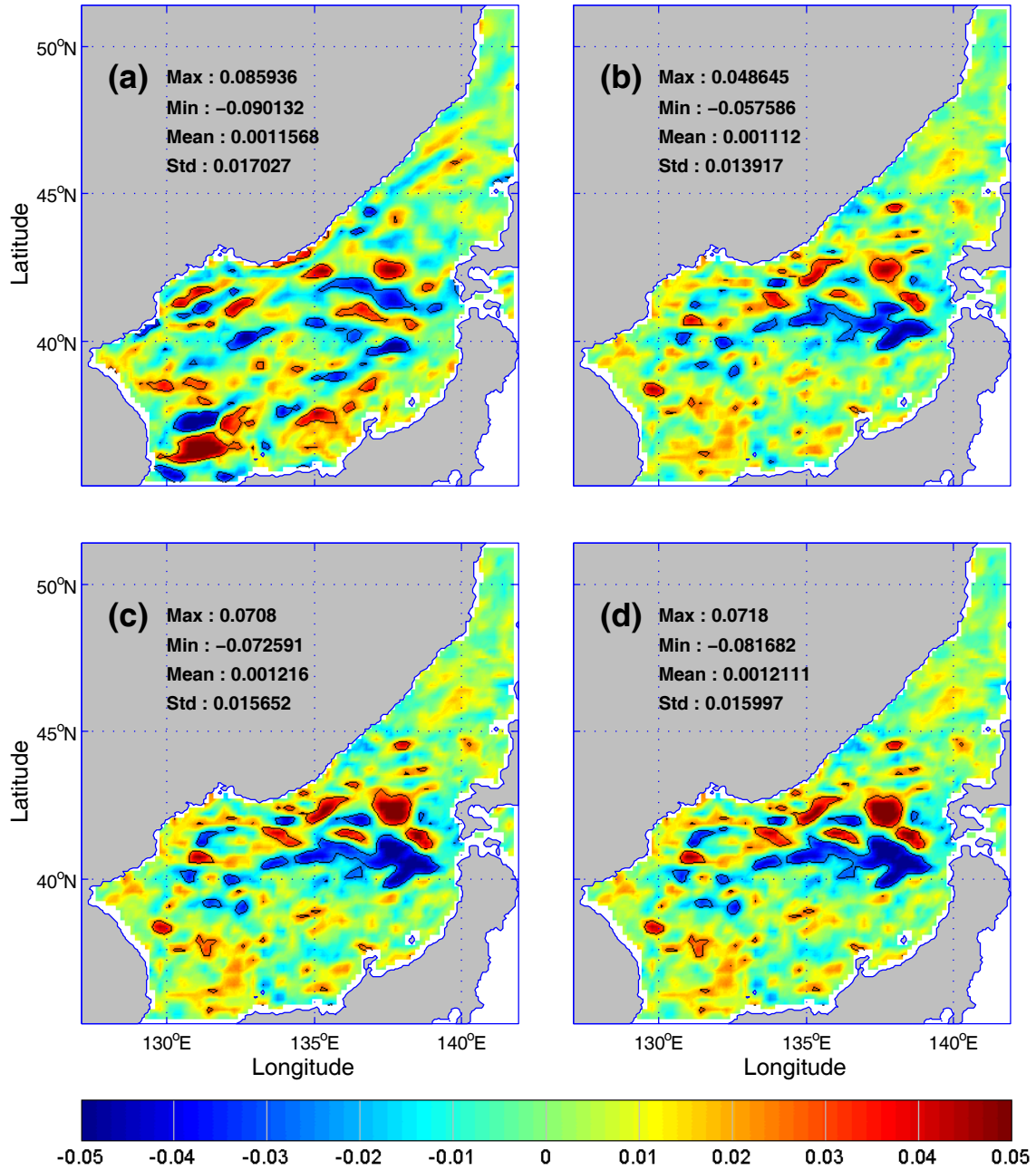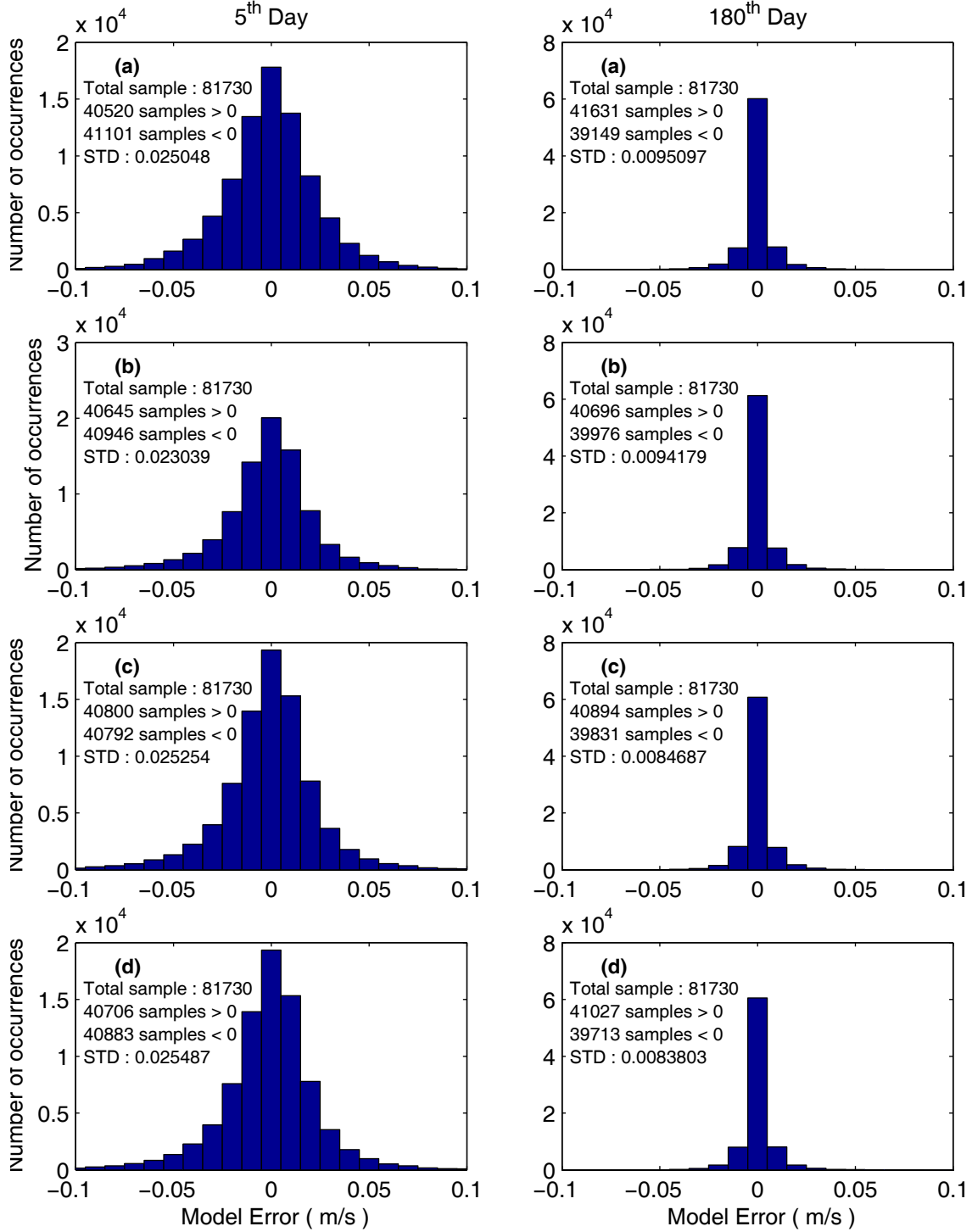
Figure 9.   Histogram of (a) Run 0 – Run 1, (b) Run 0 – Run 2, (c) Run 0 – Run 3 and (d) Run 0 – Run 4 for v component of velocity field on both the 5th and 180th day after the model integration.

2. The Root Mean Square Error (RMSE)

a. The Vertical Variation

The Root Mean Square Error (RMSE), calculated by equation (12), is commonly used to evaluate the model performance. For the vertical profile of RMSE, two plots contained the errors caused by these four experimental runs for the horizontal velocity (**V**) fields made on the both the 5th day (day-185) and the 180th day (day-360) after the day of model integration (day-180). These plots are shown in Figure 10.

As seen in this figure, RMSE on the 5th day reveals higher value above sigma level 8, which indicates some stronger effects on model prediction occurring at those levels. The maximum RMSE occurs in Run 1 with a value of 0.056 m/s at level 1. These features are similar for the RMSE on the 180th day. The maximum RMSE occurs in Run 2 with a value of 0.02 m/s at level 1. In general, from these plots, the curves representing these four experimental runs are very close to each other, indicating no obvious difference among the effects of these four experimental runs. In addition, the RMSE of horizontal velocity (**V**) changed dramatically from the 5th day (0.05 m/s near surface level and 0.03 m/s near bottom level) to the 180th day (0.02 m/s near surface level and 0.01 m/s near bottom level).

b. The Temporal Evolution

The temporal evolution of vertically averaged *RMSE* for the horizontal velocity (**V**) fields from the 5th day to 180th day is shown in Figure 11. As seen in this figure, no significant difference shows among these four curves of RMSE for the horizontal velocity (**V**) fields. The RMSE of horizontal velocity rapidly decreases with time in the first 20 days from a peak value of 0.032 m/s to 0.02 m/s. It then slowly decreases with time to 0.01 m/s on the 180th day. In general, as in the previous results, no obvious difference exists among the effects of these four experimental runs.

34

Figure 10.   RMSE of V in (a) Run 0 – Run 1, (b) Run 0 – Run 2, (c) Run 0 – Run 3 and (d) Run 0 – Run 4 on the 5th day and the 180th day after the model integration.


Figure 11.   Temporal evolution of vertically averaged RMSE of V in a) Run 0 – Run 1, (b) Run 0 – Run 2, (c) Run 0 – Run 3 and (d) Run 0 – Run 4.

3. The Relative Root Mean Square Error (RRMSE)

a. *The Vertical Variation*

The Relative Root Mean Square Error (RRMSE), calculated by equation (13), is also commonly used for evaluating model performance. For the vertical profile of RRMSE, two plots contained the errors caused by these four experimental runs for the horizontal velocity (**V**) fields made on both the 5th day (day-185) and the 180th day (day-360) after the day of model integration (day-180). These plots are shown in Figure 12.

As seen in this figure, the RRMSE on the 5th day reveals a higher value below sigma level 18, which indicates some stronger effects on model prediction occurring at those levels. The maximum RRMSE occurs in Run 1 with a value of 0.75 at level 22. On the other hand, the RRMSE on the 180th day reveals a higher value above sigma level 8, which indicates some stronger effects on model prediction occurring at those levels. The maximum RRMSE occurs in Run 2 with a value of 0.26 at level 4. In general, from these plots, the curves representing these four experimental runs are very close to each other, indicating no obvious difference among the effects of these four experimental runs. Similar to previous plots of the RMSE, the RRMSE of horizontal velocity (**V**) changed dramatically from the 5th day (0.7 near surface level and 0.5 near bottom level) to the 180th day (0.25 near surface level and 0.2 near bottom level).

b. *The Temporal Evolution*

The temporal evolution of vertically averaged RRMSE for the horizontal velocity (**V**) fields from the 5th day to the 180th day is shown in Figure 13. As seen in this figure, no significant difference exists among these four curves of the RRMSE for the horizontal velocity (**V**) fields. The RRMSE of horizontal velocity rapidly decreases with time in the first 20 days from a peak value of 0.5 to 0.3 and then slowly decreases with time to 0.2 on the 180th day. In general, no obvious difference among the effects of these four experimental runs exists. Notably, the RRMSE of horizontal velocity was between 0.3 and 0.5. Therefore, the effects of the velocity initialization processes to the model horizontal velocity prediction are quite significant.
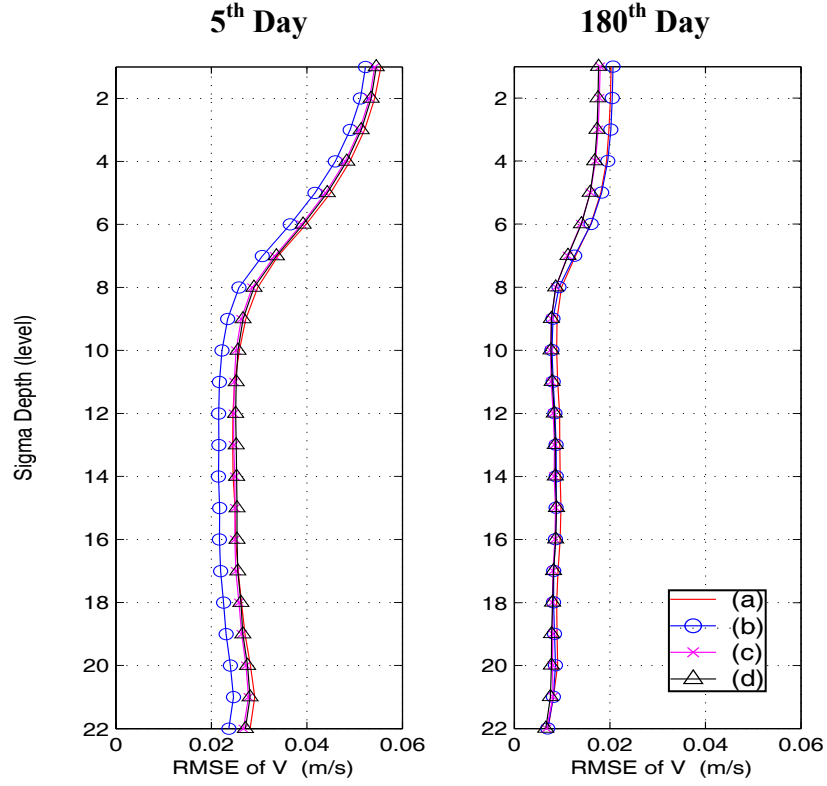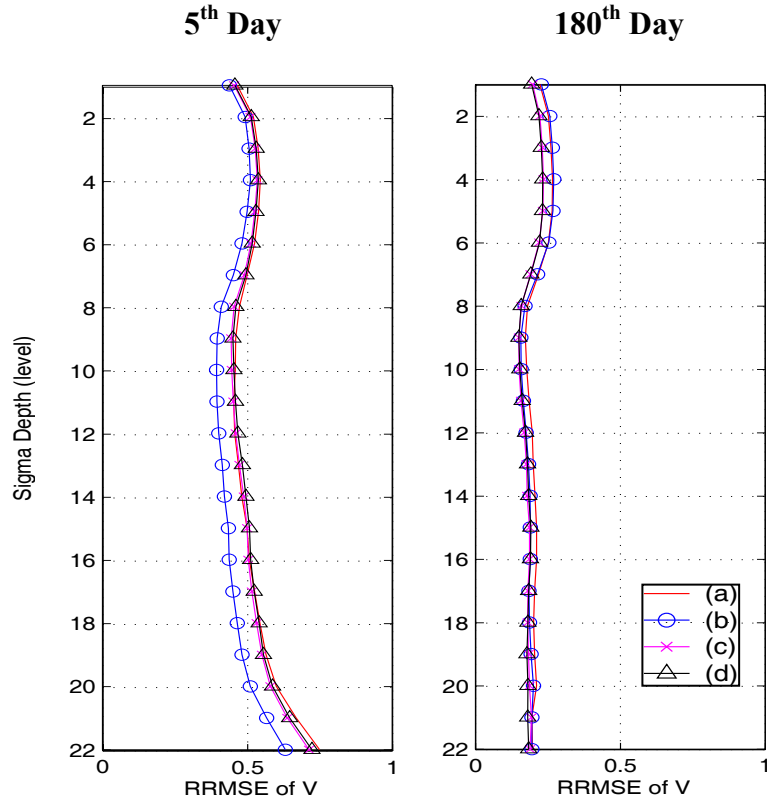
5th Day   **180th Day**

Figure 12.   RRMSE of V in (a) Run 0 – Run 1, (b) Run 0 – Run 2, (c) Run 0 – Run 3 and (d) Run 0 – Run 4 on the 5th day and the 180th day after the model integration.
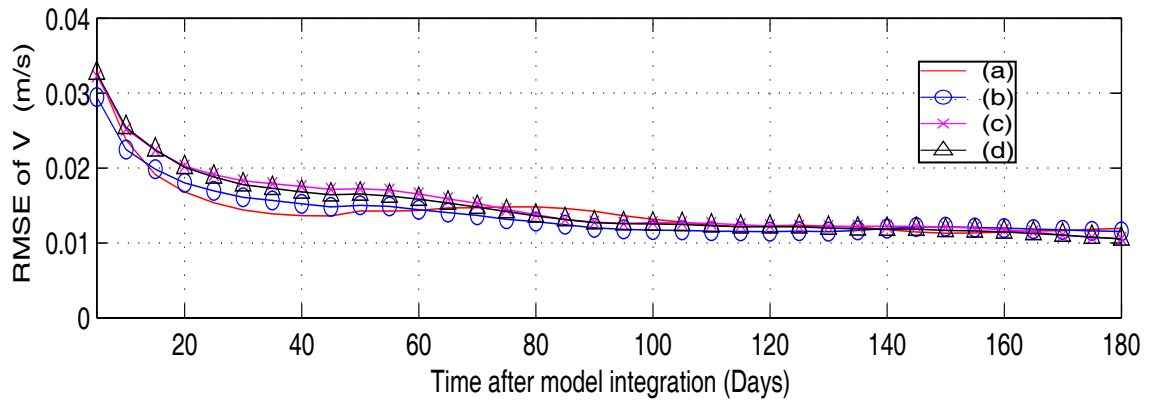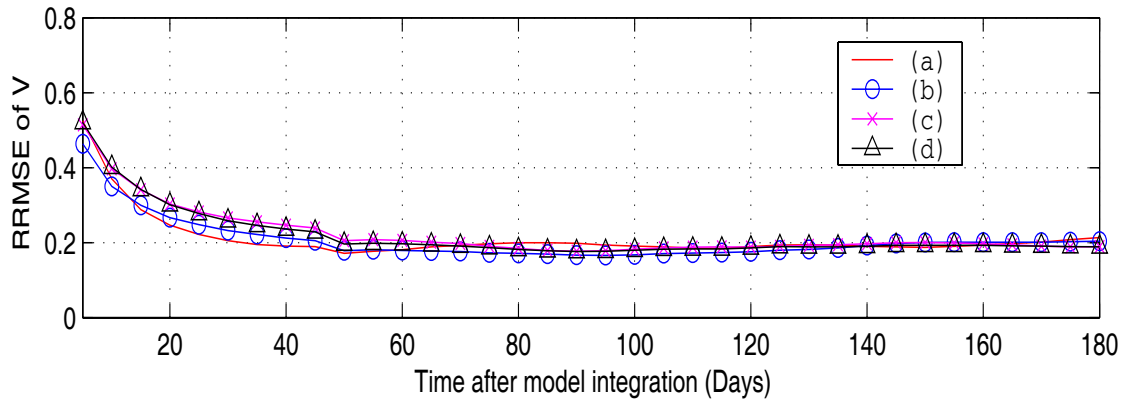

Figure 13.   Temporal evolution of vertically averaged RRMSE of V in (a) Run 0 – Run 1, (b) Run 0 – Run 2, (c) Run 0 – Run 3 and (d) Run 0 – Run 4.

B.   WIND FORCING

1.   The Model Error

a.   *The Horizontal Distribution*

As mentioned in section A, after the model error was calculated, for each horizontal grid point, the errors for all the 22 sigma levels were combined vertically for each field on the 5th day (day-185) and the 180th day (day-360) after the day of model integration (day-180). Four plots contained the horizontal distribution of these vertically mean model errors for each specific field (*u* and *v*) between the control run and two experimental runs (Run 5 and Run 6) made on both the 5th day and 180th day. The values of max, min, mean and standard deviation were also determined for each plot. These plots are shown in Figure 14 to 15.

As seen in these figures, the model errors of both u and v on the 5th and 180th days reveal that numerous small- to meso-scale patterns of negative and positive model errors are distributed near the Japan Basin and some of the coastal areas of JES. As expected, for the model errors on the 5th day, relatively strong patterns are present in Run 6 with relatively high values of the maximum, minimum, mean and standard deviation. A significant difference in these statistic values exists between the two experimental runs. These features are similar for the model errors on the 180th day. These relatively strong patterns are also present in Run 6 with the higher statistic values. This indicates the model error caused by Run 6 had a larger effect on the model performance than that caused by the Run 5. As observed, the model errors are present mostly near the Japan Basin. This could be associated with the nearby Polar Front (PF) where two current systems (NKCC and TWC) converge. In general, from these horizontal distribution plots, obvious differences exist between Run 5 and Run 6 (more model error was caused by Run 6). In addition, the model errors increase slowly from the 5th to the 180th day.

38

b.   *The Histogram*

The model error, calculated by equation (11), is also present in the form of a histogram in evaluating the model error distribution. Two histogram plots contained the model errors on each specific field (*u* and *v*) between the control run and two experimental runs made on the 5th day and the 180th day. The values of the number of the total sample, samples greater than zero, samples less than zero and standard deviation were also determined for each plot. These plots are shown in Figure 16 to 17.

In Figure 16, the histogram of model errors of *u* components of the horizontal velocity on both the 5th day and 180th day reveals a Gaussian-type distribution on each plot. Similar to previous plots, the values of standard deviation (STD) are higher in Run 6 than those in Run 5 and they increase with integration time on each experimental run. For the 5th day, the maximum and minimum values of standard deviation occur in Run 6 and Run 5 with a value of 0.015 m/s and 0.009 m/s, respectively. For the 180th day, the maximum and minimum values of standard deviation also occur in Run 6 and Run 5 with a value of 0.016 m/s and 0.01 m/s, respectively. These features are similar for the histogram of model errors of *v* components of the horizontal velocity on both the 5th day and 180th day in Figure 17. Again, for both the 5th and 180th day, the maximum and minimum values of standard deviation occur in Run 6 and Run 5 with the maximum and minimum value of 0.017 m/s and 0.001 m/s on the 5th day, and 0.018 m/s and 0.001 m/s on the 180th day, respectively. Generally speaking, the differences between Run 5 and Run 6 (more model error was caused by Run 6) are quite significant while these model errors increase slightly from the 5th day to the 180th day.

5th Day

180th Day

(a) Max : 0.023536
Min : −0.020814
Mean : 6.548e−005
Std : 0.003555

(a) Max : 0.027295
Min : −0.017191
Mean : 0.00017596
Std : 0.0044493

(b) Max : 0.042123
Min : −0.038718
Mean : 0.0003849
Std : 0.0062038

(b) Max : 0.044023
Min : −0.030114
Mean : 0.00057764
Std : 0.0073368
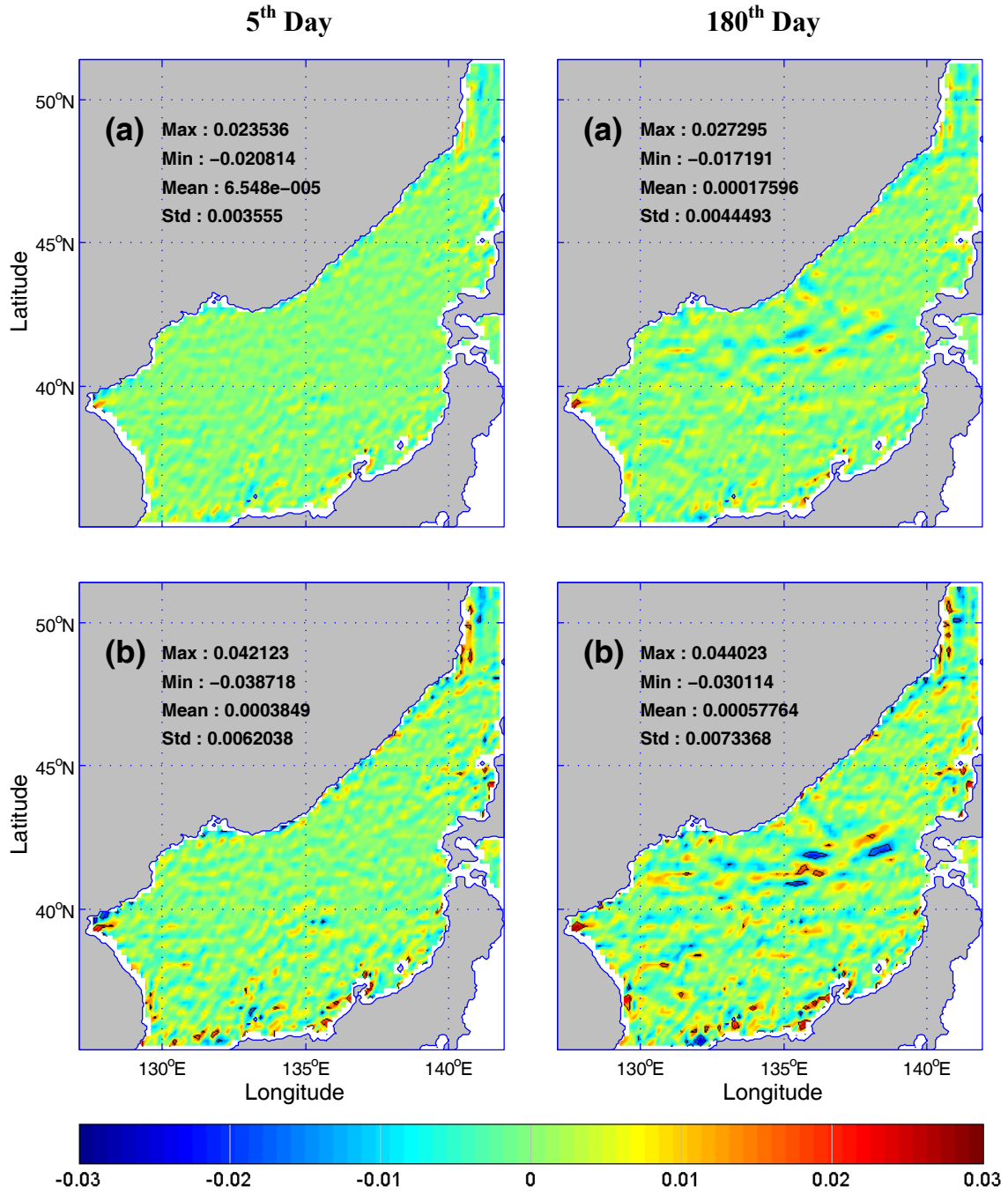
Figure 14.   Vertically averaged model error of (a) Run 0 – Run 5 and (b) Run 0 – Run 6 for u component of velocity field on both the 5th day and 180th day after the model integration.

40

5th Day   **180th Day**

Figure 15.   Vertically averaged model error of (a) Run 0 – Run 5 and (b) Run 0 – Run 6 for v component of velocity field on both the 5th day and 180th day after the model integration.
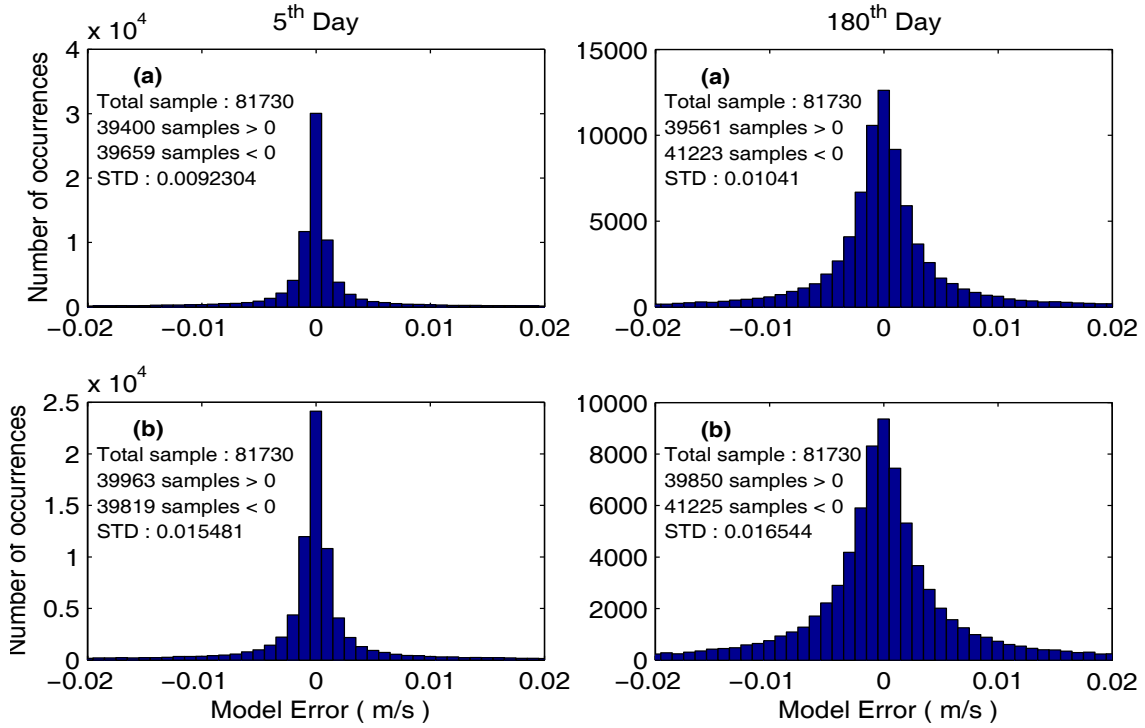
Figure 16. Histogram of (a) Run 0 – Run 5 and (b) Run 0 – Run 6 for u component of velocity field on both the 5th and 180th day after the model integration.
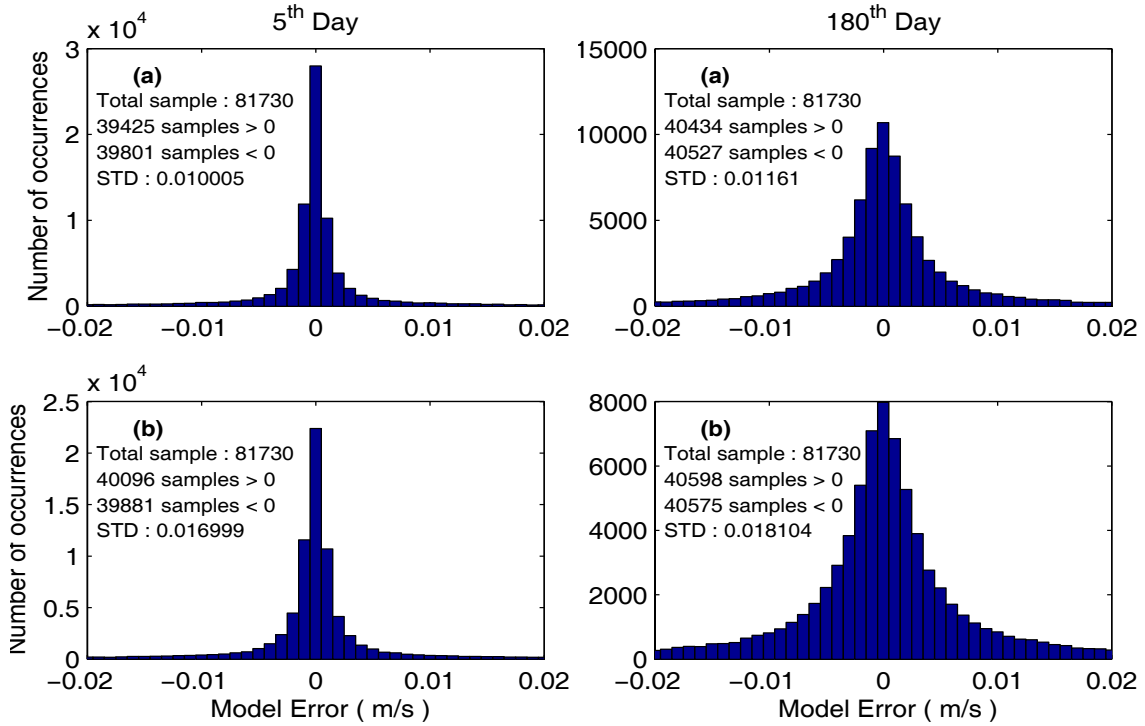
Figure 17. Histogram of (a) Run 0 – Run 5 and (b) Run 0 – Run 6 for v component of velocity field on both the 5th and 180th day after the model integration.

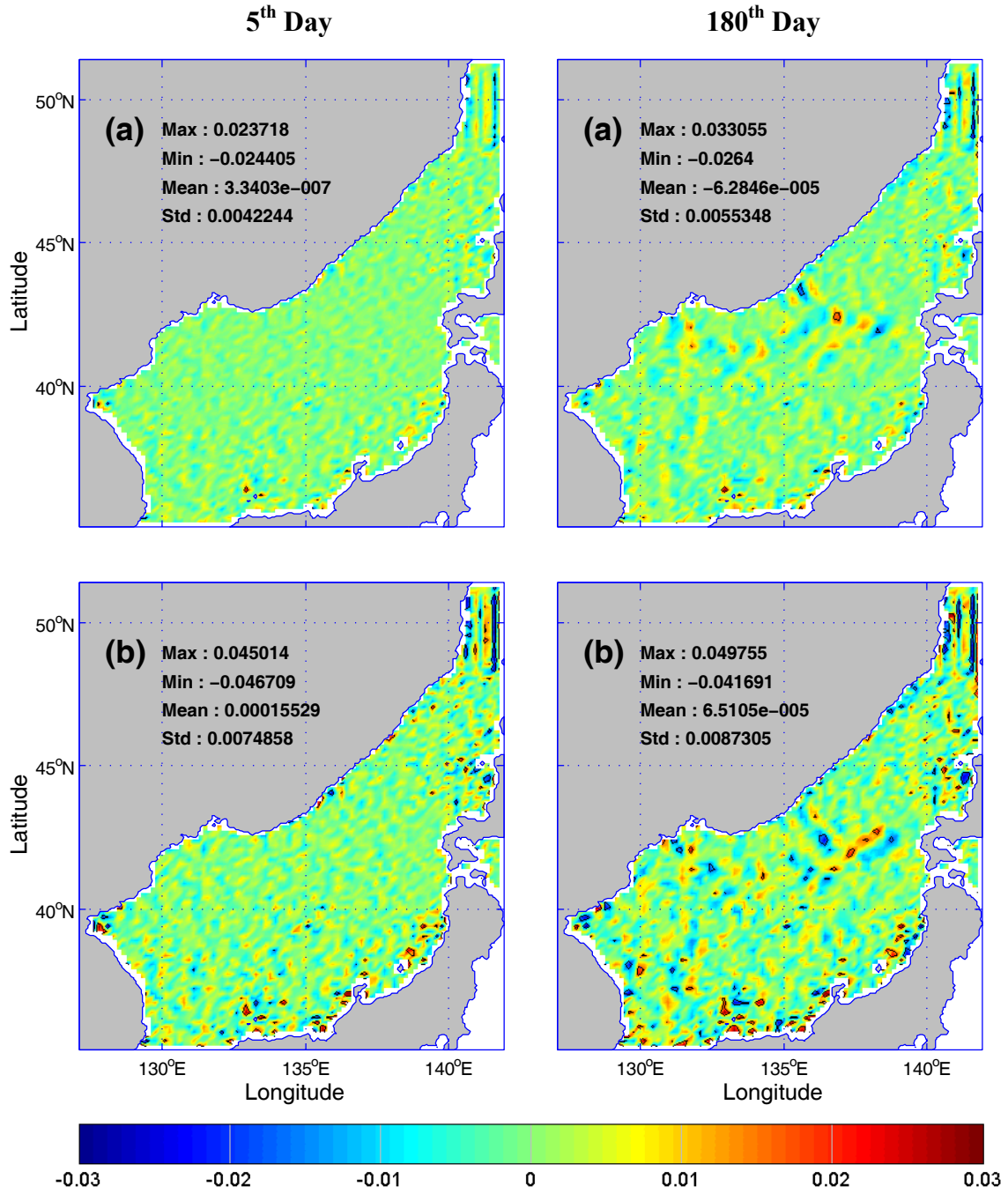## 2.   The Root Mean Square Error (RMSE)

a.   *The Vertical Variation*

The Root Mean Square Error calculated by equation (12) evaluates the model performance. For the vertical profile of RMSE, two plots contained the errors caused by these two experimental runs for the horizontal velocity (**V**) fields made on both the 5th day (day-185) and the 180th day (day-360) after the day of model integration (day-180). These plots are shown in Figure 18.

As seen in this figure, the RMSE on the 5th day reveals a higher value occurring above sigma level 8, which indicates that some stronger effects on model prediction occurring at those levels. The maximum RMSE occurs in Run 6 at level 1 with a value of 0.068 m/s. These features are similar for the RMSE on the 180th day. As expected, the maximum RMSE of horizontal velocity occurs in Run 6 at level 1 with a value of 0.07 m/s. In general, from these plots, obvious differences exist between the RMSE in Run 5 and Run 6 (more RMSE was caused by Run 6) increasing slowly from the 5th day to the 180th day. In addition, these values of RMSE decrease with depth (rapidly above sigma level 8).

b.   *The Temporal Evolution*

The temporal evolution of vertically averaged RMSE for horizontal velocity (**V**) fields from the 5th day to 180th day is shown in Figure 19. As the figure demonstrates, significant differences among these two curves of RMSE are evident for the horizontal velocity (**V**) fields (more RMSE was caused by Run 6). The RMSE increases with time in the first 45 days and reaches a peak value of 0.018 m/s and 0.011 m/s in Run 6 and Run 5, respectively. It then rapidly decreases from the 45th day to the 60th day. The changes are little between the 60th day and the 130th day, but they increase again from the 130th day to the 180th day. For Run 6 and Run 5, the increased value from the 5th day to the 180th day is 0.003 m/s and 0.002 m/s, respectively. In general, just like the other previous results, obvious differences occur between the RMSE in Run 5 and Run 6 (more RMSE was caused by Run 6) increasing from the 5th day to the 180th day.

43

5th Day　　　　**180th Day**

Figure 18.　　RMSE of V in (a) Run 0 – Run 5 and (b) Run 0 – Run 6 on the 5th day and the 180th day after the model integration.

Figure 19.　　Temporal evolution of vertically averaged RMSE of V in (a) Run 0 – Run 5 and (b) Run 0 – Run 6.

3.   The Relative Root Mean Square Error (RRMSE)

a.   *The Vertical Variation*

The Relative Root Mean Square Error, calculated by equation (13), is also commonly used when evaluating the model performance. For the vertical profile of RRMSE, two plots contained the errors caused by these two experimental runs for the horizontal velocity (**V**) fields made on both the 5th day (day-185) and the 180th day (day-360) after the day of model integration (day-180). These plots are shown in Figure 20.

As seen in this figure, the RRMSE on the 5th day reveals a higher value above sigma level 8, which indicates some stronger effects on model prediction occurring at those levels. The maximum RRMSE occurs in Run 6 with a value of 0.58 at level 1 for horizontal velocity. The RRMSE on the 180th day also reveals a higher value above sigma level 8, which indicates some stronger effects on model prediction occurring at those levels. As expected, the maximum RRMSE occurs in Run 6 with a value of 0.76 at level 1 for horizontal velocity. In general, from these plots, the RRMSE caused by Run 6 is larger than that caused by Run 5 on both days. Generally, the RRMSE decreases with depth (rapidly above sigma level 8). As observed, the effect of the wind forcing noise on the model velocity field prediction is significant, especially above sigma level 8 (around 60 % and 35 % on the 5th day and 80 % and 50 % on the 180th day at the surface level in Run 6 and Run 5, respectively).

b.   *The Temporal Evolution*

The temporal evolution of vertically averaged RRMSE for horizontal velocity (**V**) fields from the 5th day to the 180th day is shown in Figure 21. As seen in this figure, significant differences exist between these two curves of RRMSE for the horizontal velocity (**V**) fields (more RRMSE was caused by Run 6). The RRMSE increases with time slowly in the first 45 days and then decreases rapidly from the 45th day to the 60th day. These changes are little between the 60th day and the 120th day but then increase again from the 130th day to the 180th day. The maximum and minimum RRMSE of horizontal velocity is 0.28 and 0.12 in Run 6 and 0.19 and 0.08 in Run 5,

respectively. As in previous results, obvious differences take place between the RRMSE in Run 5 and Run 6 (more RRMSE was caused by Run 6) increasing from the 5th day to the 180th day.
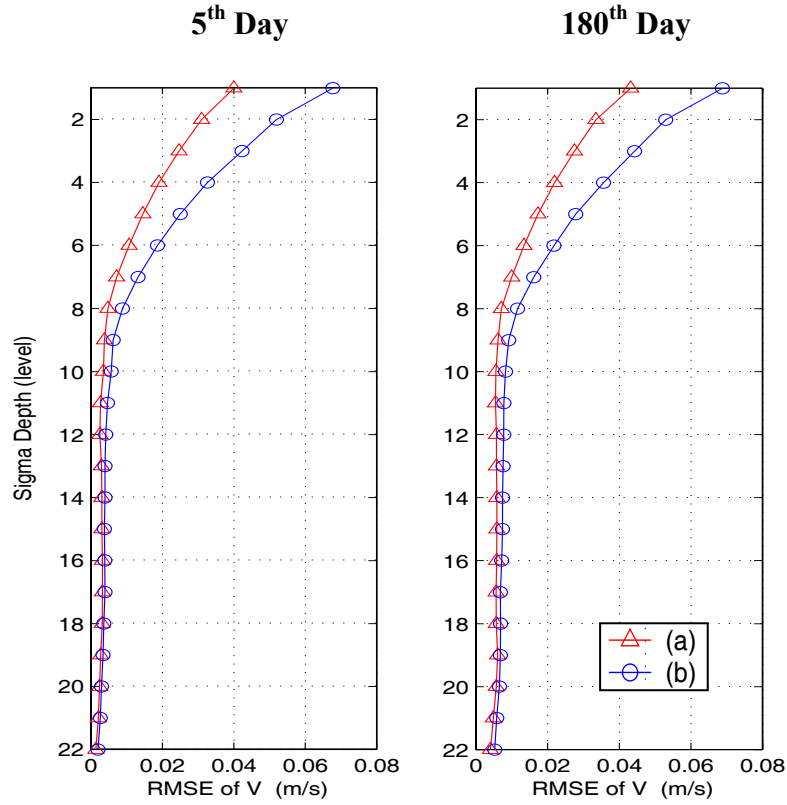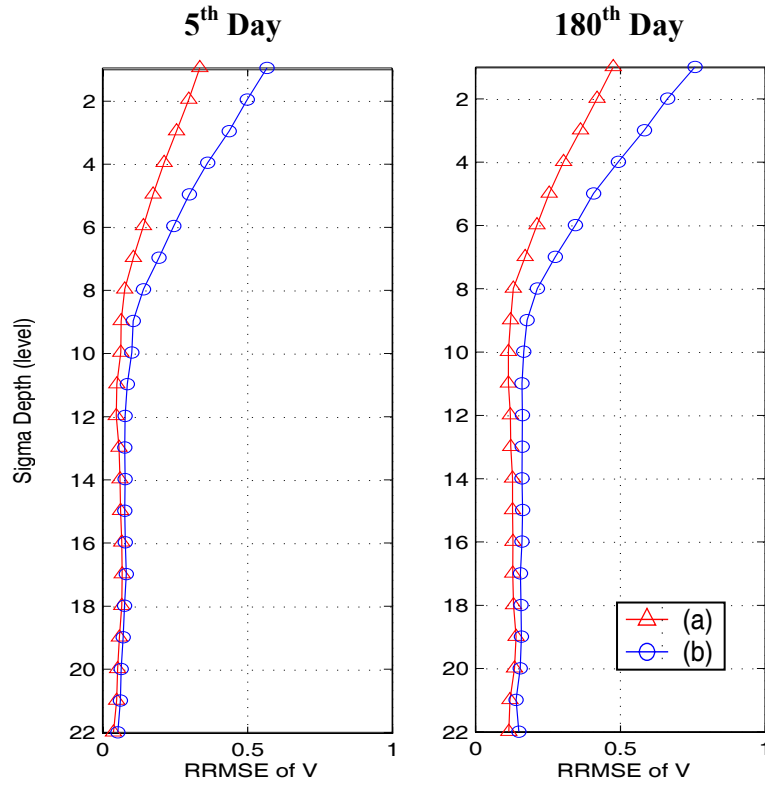
5th Day

180th Day

Figure 20. RRMSE of V in (a) Run 0 – Run 5 and (b) Run 0 – Run 6 on the 5th day and the 180th day after the model integration.

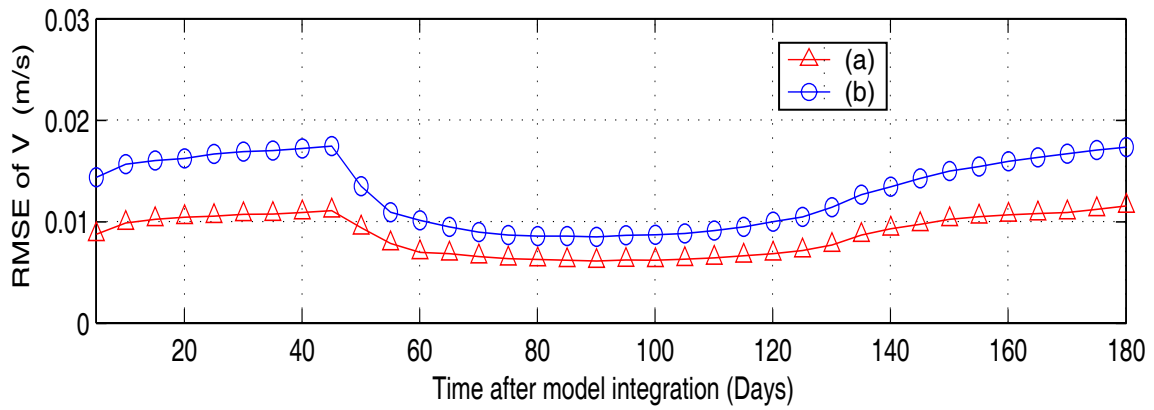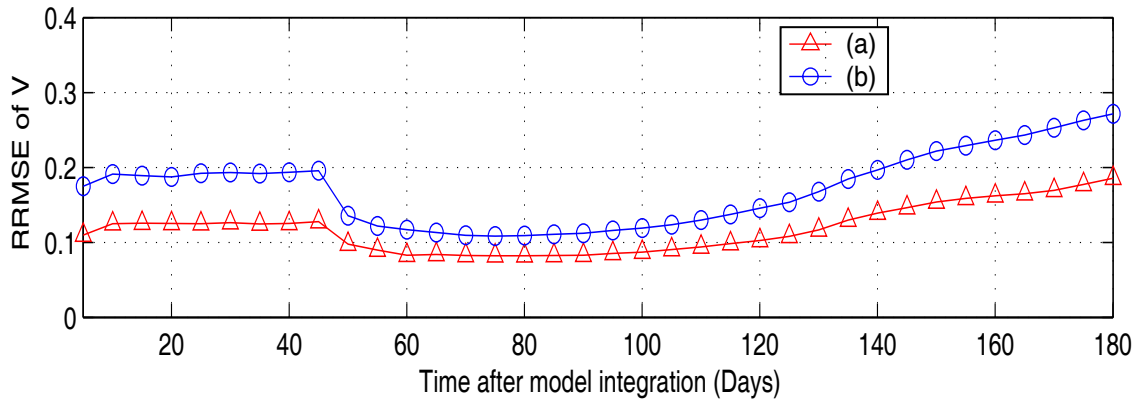

Figure 21. Temporal evolution of vertically averaged RRMSE of V in (a) Run 0 – Run 5 and (b) Run 0 – Run 6.

C.   OPEN BOUNDARY CONDITIONS

1.   The Model Error

a.   The Horizontal Distribution

As mentioned in section A, after the model error was calculated, for each horizontal grid point, the errors for all the 22 sigma levels were combined vertically for each field on the 5th day (day-185) and the 180th day (day-360) after the day of model integration (day-180). Four plots contained the horizontal distribution of these vertically mean model errors in each specific field (u and v) between the control run and two experimental runs (Run 7 and Run 8) made on the 5th day and the 180th day. The values of max, min, mean and standard deviation were also determined for each plot. These plots are shown in Figure 22 to 23.

As seen in these figures, model errors of both u and v on the 5th and the 180th day reveal that only a few small-scale patterns occur near the Tatar Strait and the Soya Strait on the 5th day; however, some small- to meso-scale patterns of model errors are present near the Tatar Strait and the Japan Basin on the 180th day. For the model errors on the 5th day, relatively strong patterns are present in Run 8 with relatively high values of the maximum, minimum, mean and standard deviation. These features are similar for the model errors on the 180th day with increased statistic values. These relatively strong patterns are also present in Run 8 with the higher statistic values. This indicates that the model error caused by Run 8 had a larger effect on the model performance than that caused by Run 7. In general, from these horizontal distribution plots, obvious differences between Run 7 and Run 8 exist (more model error was caused by Run 8) with the model errors also increasing from the 5th to the 180th day.

b.   The Histogram

The model error, calculated by equation (11), is also present in the form of a histogram when evaluating the model error distribution. Two histogram plots contained the model errors on each specific field (u and v) between the control run and two

experimental runs made on the 5th day and the 180th day. The values of the number of the total sample, samples greater than zero, samples less than zero and standard deviation were also determined for each plot. These plots are shown in Figure 24 to 25.

In Figure 24, the histogram of model errors of u components of the horizontal velocity on both the 5th day and 180th day reveals a Gaussian-type distribution on each plot. Similar to the previous plots, the values of standard deviation (STD) are higher in Run 8 than those in Run 7 increasing with integration time on each experimental run. For the 5th day, the maximum and minimum values of standard deviation occur in Run 8 and Run 7 with a value of 0.006 m/s and 0.003 m/s, respectively. For the 180th day, the maximum and minimum values of standard deviation also occur in Run 8 and Run 7 with a value of 0.008 m/s and 0.005 m/s, respectively. These features are similar for the histogram of model errors of v components of the horizontal velocity on both the 5th day and the 180th day in Figure 25. Once again, for both the 5th and the 180th day, the maximum and minimum values of standard deviation occur in Run 8 and Run 7 with a value of 0.007 m/s and 0.004 m/s on the 5th day, and 0.009 m/s and 0.006 m/s on the 180th day, respectively. Generally speaking, these model errors increase from the 5th day to the 180th day and the differences between Run 7 and Run 8 (more model error was caused by Run 8) are significant.
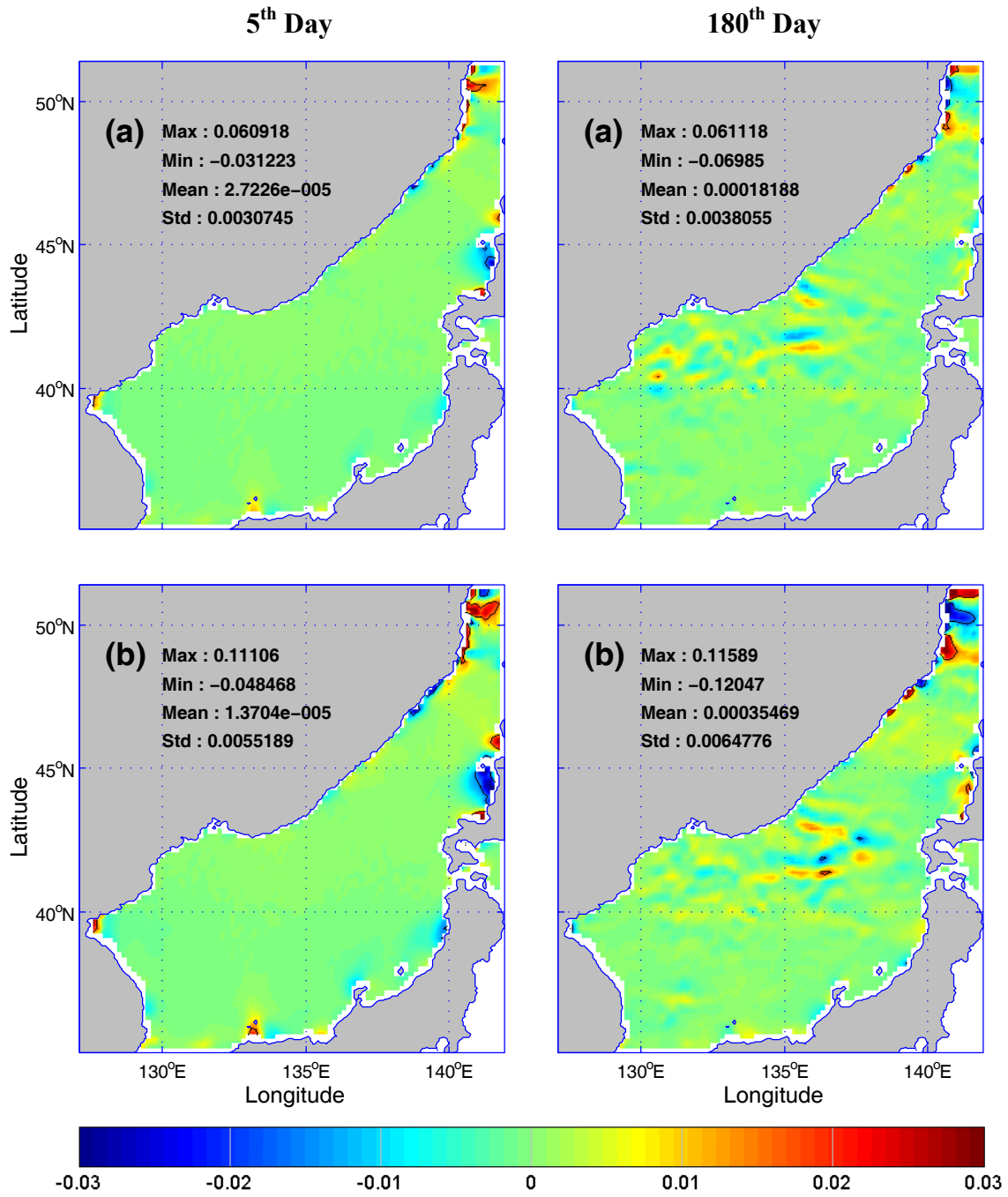
5th Day **180th Day**

Figure 22. Vertically averaged model error of (a) Run 0 – Run 7 and (b) Run 0 – Run 8 for u component of velocity field on both the 5th day and 180th day after the model integration.

5th Day

180th Day

(a) Max : 0.054023
Min : −0.074518
Mean : 0.00024396
Std : 0.003521

(a) Max : 0.078182
Min : −0.049995
Mean : 0.0001067
Std : 0.0043425

(b) Max : 0.10567
Min : −0.11751
Mean : 0.00049281
Std : 0.0062691

(b) Max : 0.15347
Min : −0.08765
Mean : 0.00029827
Std : 0.0074165

Figure 23.   Vertically averaged model error of (a) Run 0 – Run 7 and (b) Run 0 – Run 8 for v component of velocity field on both the 5th day and 180th day after the model integration.
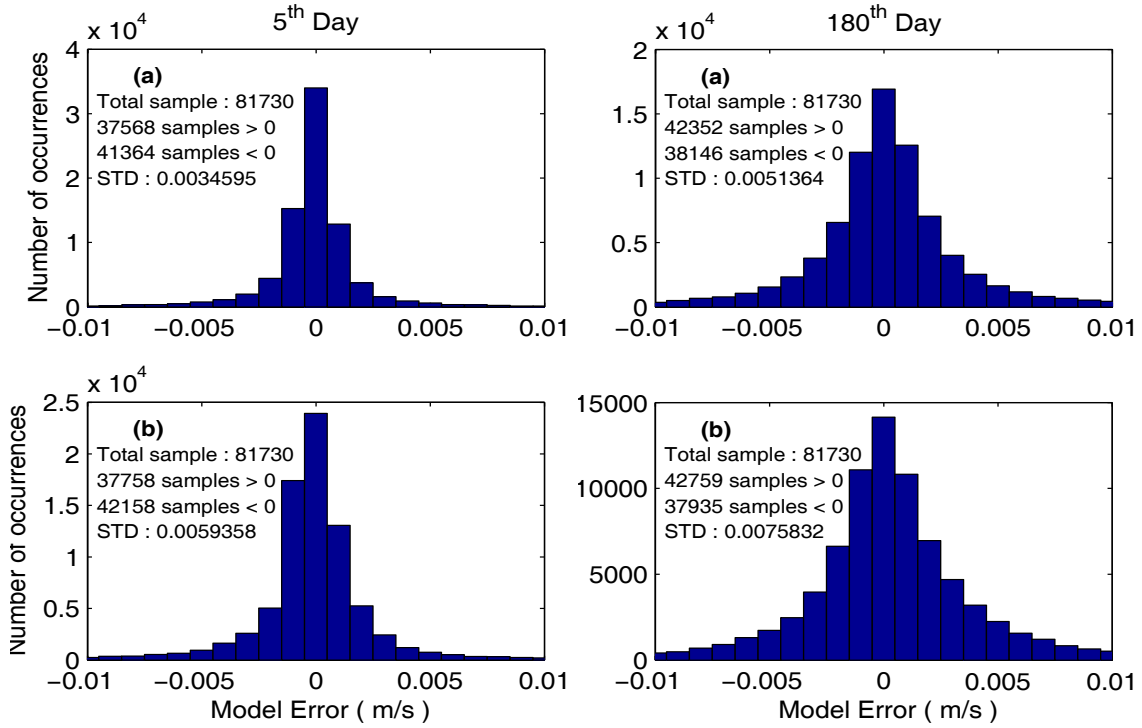
Figure 24.   Histogram of (a) Run 0 – Run 7 and (b) Run 0 – Run 8 for u component of velocity field on both the 5th and 180th day after the model integration.

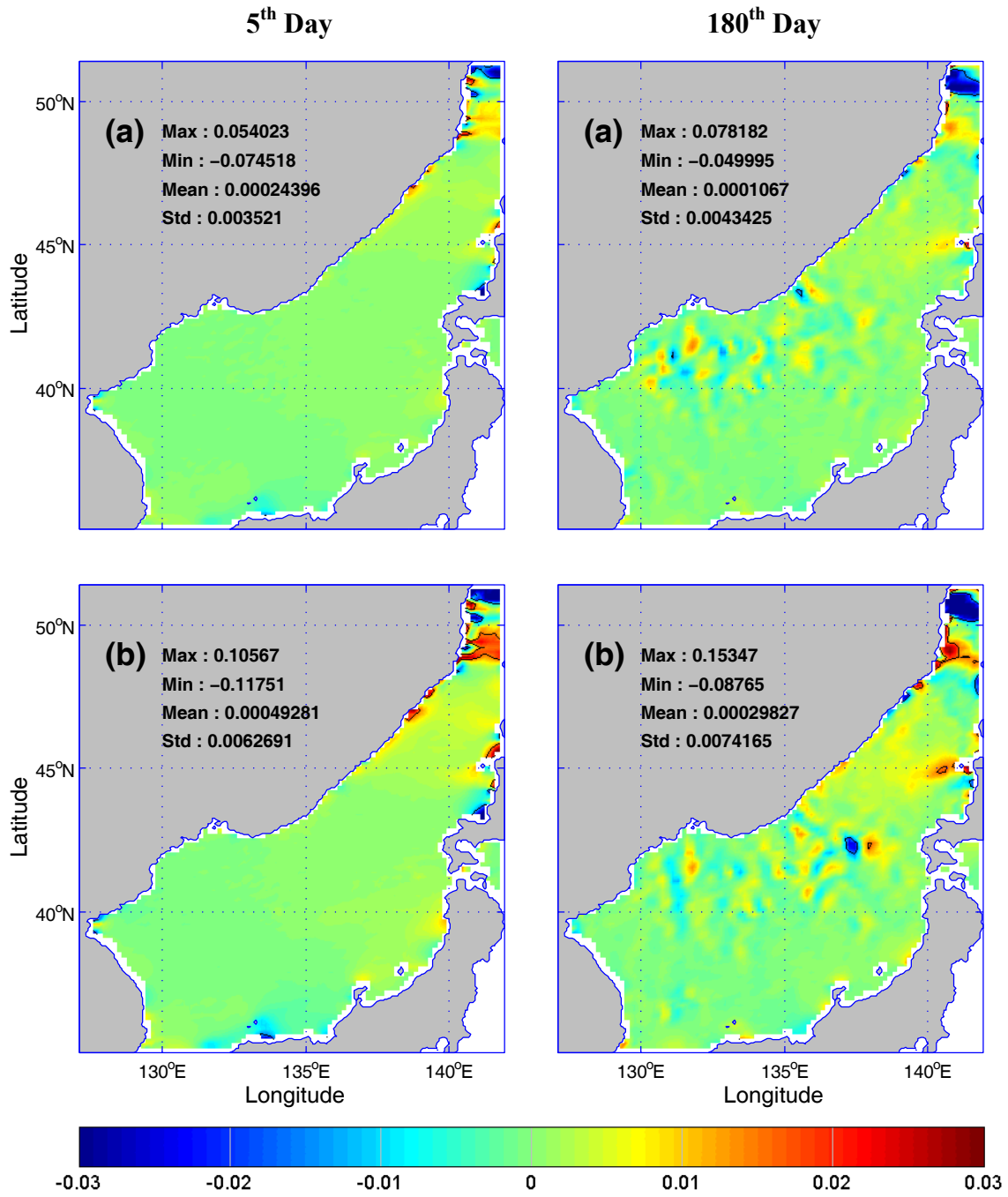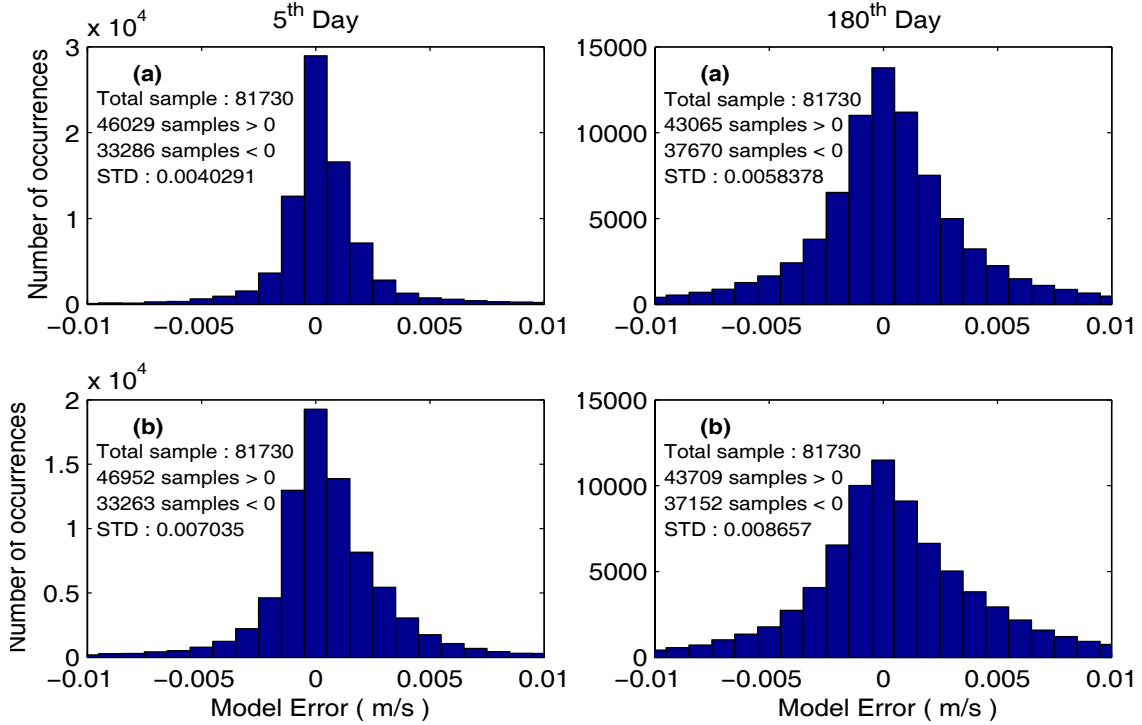Figure 25.   Histogram of (a) Run 0 – Run 7 and (b) Run 0 – Run 8 for v component of velocity field on both the 5th and 180th day after the model integration.

52

2. The Root Mean Square Error (RMSE)

a. *The Vertical Variation*

The Root Mean Square Error, calculated by equation (12), is used for evaluating the model performance. For the vertical profile of RMSE, two plots contained the errors caused by these two experimental runs for the horizontal velocity (**V**) fields made on both the 5th day (day-185) and the 180th day (day-360) after the day of model integration (day-180). These plots are shown in Figure 26.

As seen in this figure, the RMSE on the 5th day reveals that the higher value of RMSE is caused by Run 8 on both days. The maximum RMSE occurs in Run 8 with a value of 0.001 m/s at level 21. These features are similar for the RMSE on the 180th day. However, the relatively higher value shifts upward to above sigma level 8, which indicates that some stronger effects on model prediction occurs at those levels. As expected, the maximum RMSE occurs in Run 8 at level 1 with a value of 0.015 m/s. In general, from these plots, obvious differences exist between the RMSE in Run 7 and Run 8 (more RMSE are caused by Run 8) increasing from the 5th day to the 180th day (obviously above the sigma level 8).

b. *The Temporal Evolution*

The temporal evolution of vertically averaged RMSE for horizontal velocity (**V**) fields from the 5th day to the 180th day is shown in Figure 27. As seen in this figure, a significant difference exists between these two curves of RMSE for the horizontal velocity (**V**) fields (more RMSE is caused by Run 8). The RMSE of horizontal velocity oscillates and generally increases with time from the 5th day to the 90th day with a peak value of 0.022 m/s and 0.012 m/s in Run 8 and Run 7, respectively. It then oscillates and generally decreases with time from the 90th day to the 180th day. For both Run 8 and Run 7, the increased value from the 5th day to the 180th day is 0.003 m/s. As in previous results, obvious differences exist between the RMSE in Run 7 and Run 8 (more RMSE is caused by Run 8) also increasing from the 5th day to the 180th day.

Figure 26. RMSE of V in (a) Run 0 – Run 7 and (b) Run 0 – Run 8 on the 5th day and the 180th day after the model integration.

Figure 27. Temporal evolution of vertically averaged RMSE of V in (a) Run 0 – Run 7 and (b) Run 0 – Run 8.

3. The Relative Root Mean Square Error (RRMSE)

a.   The Vertical Variation

The Relative Root Mean Square Error, calculated by equation (13), is also commonly used for evaluating the model performance. For the vertical profile of RRMSE, two plots contained the errors caused by these two experimental runs for the horizontal velocity (**V**) fields made on both the 5th day (day-185) and the 180th day (day-360) after the day of model integration (day-180). These plots are shown in Figure 28.

As seen in this figure, the RRMSE on the 5th day reveals that a relatively higher value occurs below sigma level 8, which indicates some stronger effects on model prediction occurring at those levels. The higher value of RRMSE is caused by Run 8 on both days (the deeper the level, the higher the value of difference). The maximum RRMSE occurs in Run 8 with a value of 0.23 at level 22. These features are similar for the RRMSE on the 180th day. The relatively higher RRMSE occurs in Run 8. As expected, the maximum RRMSE occurs in Run 8 with a value of 0 0.28 at level 22. In general, in these plots, the RRMSE caused by Run 8 is larger than that by Run 7 on both days and increases with depth. As observed, the effects of the uncertainty on lateral boundary transport to the model velocity field prediction (8 % at level 1 and 25 % at level 22 on the 5th day and 18 % at level 1 and 28 % at level 22 on the 180th day in Run 8) are also significant.

b.   The Temporal Evolution

The temporal evolution of vertically averaged RRMSE for horizontal velocity (**V**) fields from the 5th day to 180th day is shown in Figure 29. As seen from this figure, a significant difference exists between these two curves of RRMSE for the horizontal velocity (**V**) fields (more RRMSE is caused by Run 8). The RRMSE of horizontal velocity oscillates and generally increases with time from the 5th day to the 150th day with a peak value of 0.32 and 0.2 in Run 8 and Run 7, respectively. It then oscillates and generally decreases with time from the 150th day to the 180th day. For both Run 8 and Run 7, the increased value from the 5th day to the 180th day is 0.05. As in

previous results, obvious differences exist between the RRMSE in Run 7 and Run 8 (more RRMSE is caused by Run 8), also increasing from the 5th day to the 180th day.
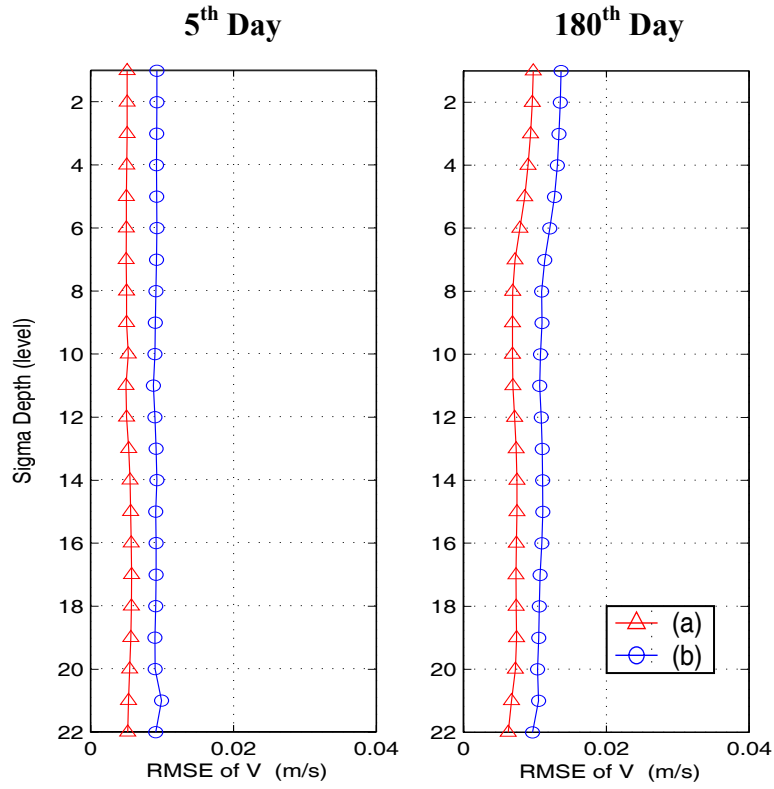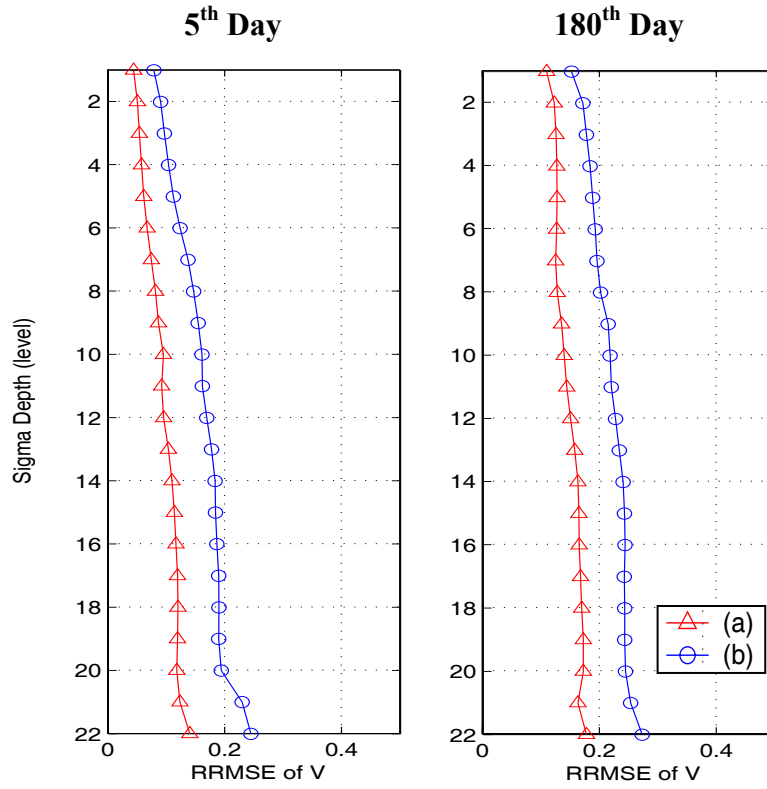
Figure 28.   RRMSE of V in (a) Run 0 – Run 7 and (b) Run 0 – Run 8 on the 5th day and the 180th day after the model integration.
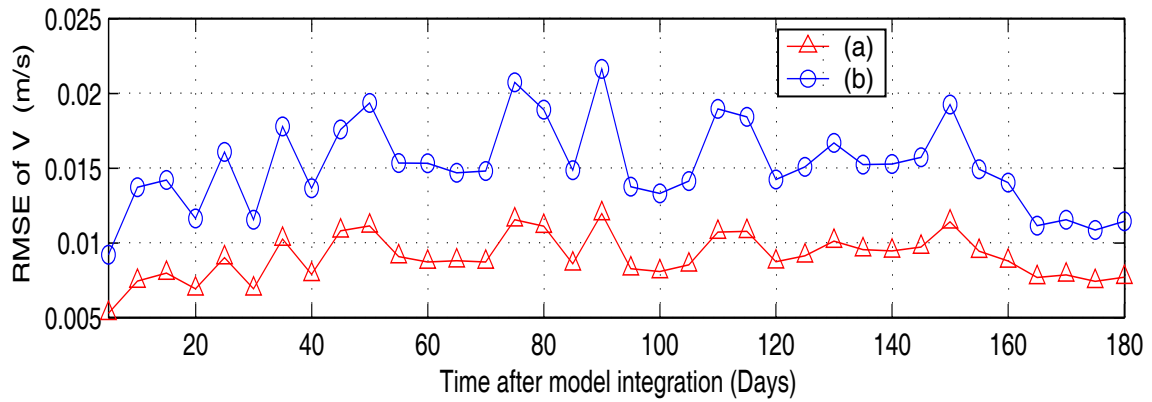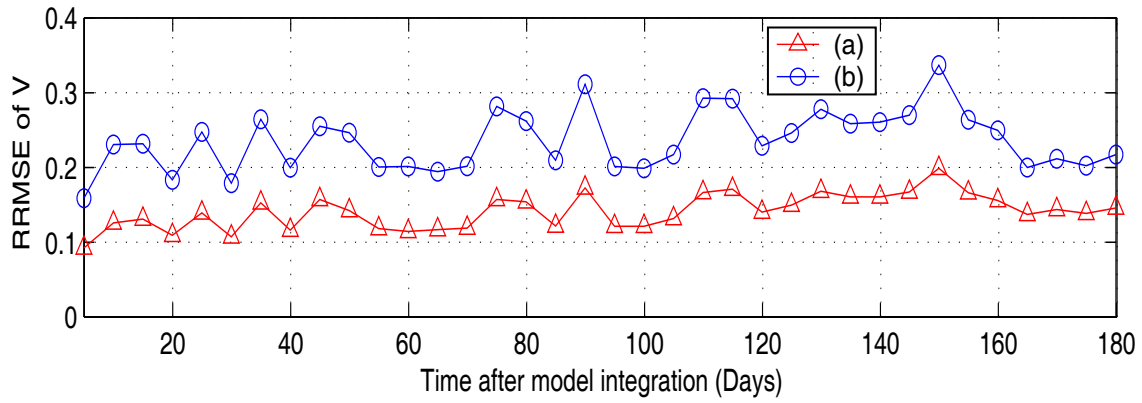

Figure 29.   Temporal evolution of vertically averaged RRMSE of V in (a) Run 0 – Run 7 and (b) Run 0 – Run 8.

D. COMBINED UNCERTAINTY

1. The Model Error

a. The Horizontal Distribution

Based on (11) derived in Chapter VI, the model error was calculated. These errors are used to measure the strength of the effect of various combined uncertainties used by these three experimental runs. After calculating the model error, for each horizontal grid point, the errors for all the 22 sigma levels were combined vertically for each field on the 5th day (day-185) and the 180th day (day-360) after the day of model integration (day-180). Six plots contained the horizontal distribution of these vertically mean model errors on each specific field (u and v) between the control run and three experimental runs (Run 9, 10 and 11) made on the 5th day and the 180th day. The values of max, min, mean and standard deviation were also determined for each plot. These plots are shown in Figure 30 to 31.

As seen in these figures, the model errors of both u and v on the 5th and the 180th days reveal that numerous small- to meso-scale patterns of negative and positive model errors are distributed near the Japan Basin and the Tatar Strait (especially on the 180th day). For the model errors on the 5th day, as expected, relatively strong patterns are present in Run 11 with relatively high statistic values of the maximum, minimum, mean and standard deviation. These features are similar for the model errors on the 180th day. These relatively strong patterns are also present in Run 11, even though the difference between Run 11 and 9 is not quite obvious. This indicates the model errors caused by Run 11 have a larger effect on the model performance than that caused by Run 9 and 10. As observed, the model errors are present mostly near the Japan Basin. This could be associated with the nearby Polar Front (PF) where two current systems (NKCC and TWC) converge. In general, from these horizontal distribution plots, obvious differences exist between each experimental run (the maximum and minimum model error is caused by Run 11 and Run 10, respectively) with the model errors decreasing obviously from the 5th to the 180th day.

58

b.   *The Histogram*

The model error, calculated by equation (11), could be presented in the form of a histogram in evaluating the model error distribution. Three histogram plots contained the model errors on each specific field (u and v) between the control run and three experimental runs made on each 5th day and 180th day. The values of the number of the total sample, samples greater than zero, samples less than zero and standard deviation were also determined for each plot. These plots are shown in Figure 32 to 33.

In Figure 32, the histogram of model errors of u components of the horizontal velocity on both the 5th day and the 180th day also reveals a Gaussian-type distribution on each plot. Similar to previous plots, the values of standard deviation (STD) are higher in Run 11 than those in Run 9 and 10, and they decrease with integration time on each experimental run. For the 5th day, the maximum and minimum values of standard deviation occur in Run 11 and Run 10 with a value of 0.026 m/s and 0.022 m/s, respectively. For the 180th day, the maximum and minimum values of standard deviation also occur in Run 11 and Run 10 with a value of 0.018 m/s and 0.01 m/s, respectively. These features are similar for the histogram of model errors of v components of the horizontal velocity on both the 5th day and the 180th day in Figure 33. Once again, for both the 5th and the 180th day, the maximum and minimum values of standard deviation occur in Run 11 and Run 10 with the maximum and minimum value of 0.029 m/s and 0.024 m/s on the 5th day and 0.02 m/s and 0.012 m/s on the 180th day, respectively. General speaking, the model error caused by Run 11 has the largest effect on model performance among these three experimental runs.

59

5ᵗʰ Day ... **180ᵗʰ Day**

(a) Max : 0.054277
Min : −0.062264
Mean : 0.0014517
Std : 0.01508

(a) Max : 0.042664
Min : −0.037759
Mean : 0.00060193
Std : 0.0080028

(b) Max : 0.10902
Min : −0.058005
Mean : 0.0011283
Std : 0.014891

(b) Max : 0.11536
Min : −0.12089
Mean : 0.00037441
Std : 0.0077715

(c) Max : 0.10593
Min : −0.062864
Mean : 0.0014561
Std : 0.015937

(c) Max : 0.12156
Min : −0.10495
Mean : 0.00098473
Std : 0.010026

Figure 30. Vertically averaged model error of (a) Run 0 – Run 9, (b) Run 0 – Run 10 and (c) Run 0 – Run 11 for u component of velocity field on both the 5ᵗʰ and 180ᵗʰ day after the model integration.

5th Day **180th Day**

(a) Max : 0.077677
Min : −0.094527
Mean : −0.001362
Std : 0.017535

(a) Max : 0.050891
Min : −0.060405
Mean : 8.6797e−005
Std : 0.010036

(b) Max : 0.10334
Min : −0.12157
Mean : −0.0011056
Std : 0.017255

(b) Max : 0.15346
Min : −0.088173
Mean : 0.00028415
Std : 0.0090885

(c) Max : 0.095259
Min : −0.11225
Mean : −0.00085382
Std : 0.018541

(c) Max : 0.15075
Min : −0.094123
Mean : 0.00043276
Std : 0.01193

Figure 31. Vertically averaged model error of (a) Run 0 – Run 9, (b) Run 0 – Run 10 and (c) Run 0 – Run 11 for v component of velocity field on both the 5th and 180th day after the model integration.

61

Figure 32.   Histogram of (a) Run 0 – Run 9, (b) Run 0 – Run 10 and (c) Run 0 – Run 11 for u component of velocity field on both the 5th and 180th day after the model integration.
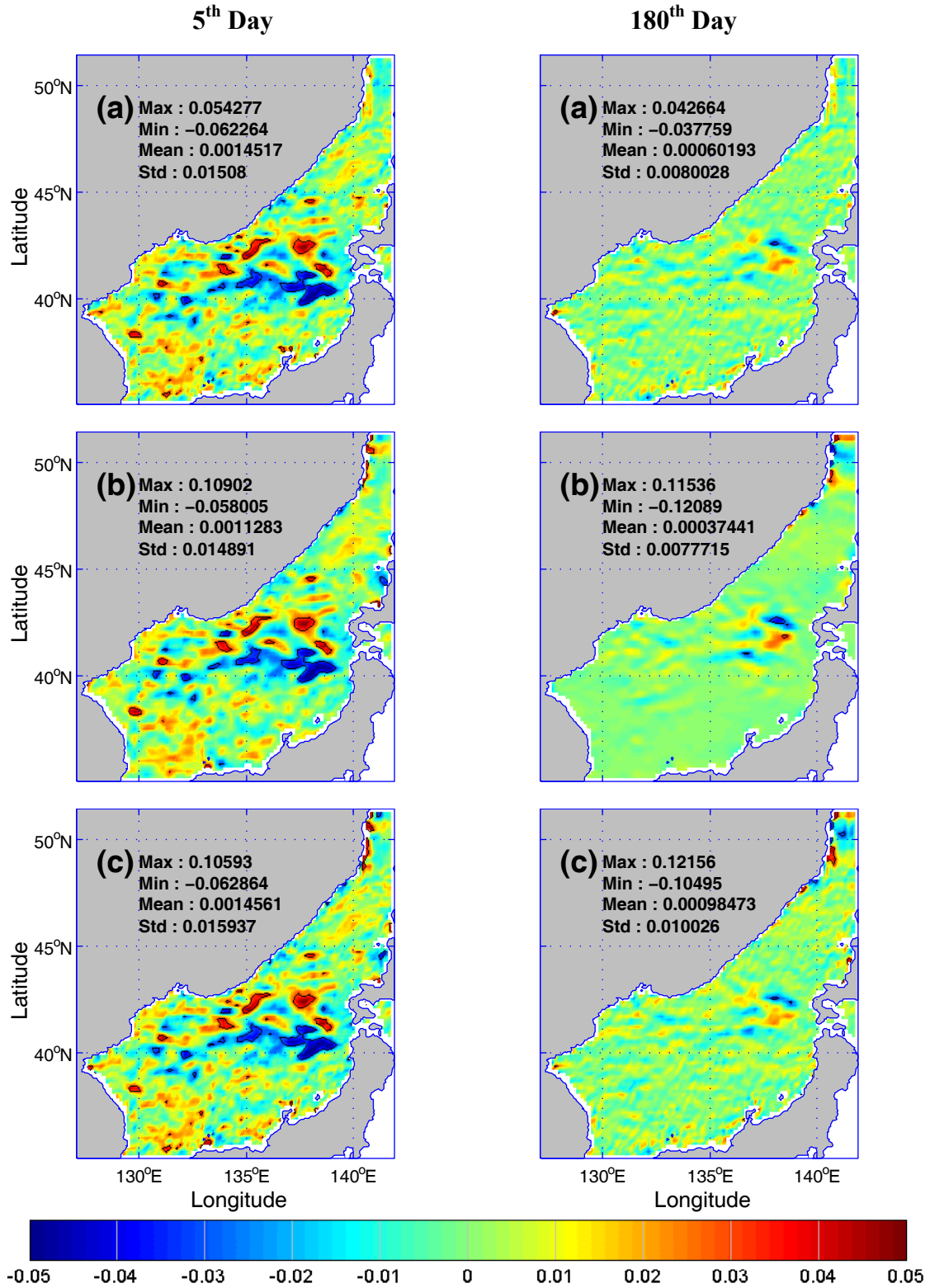
Figure 33.   Histogram of (a) Run 0 – Run 9, (b) Run 0 – Run 10 and (c) Run 0 – Run 11 for v component of velocity field on both the 5th and 180th day after the model integration.
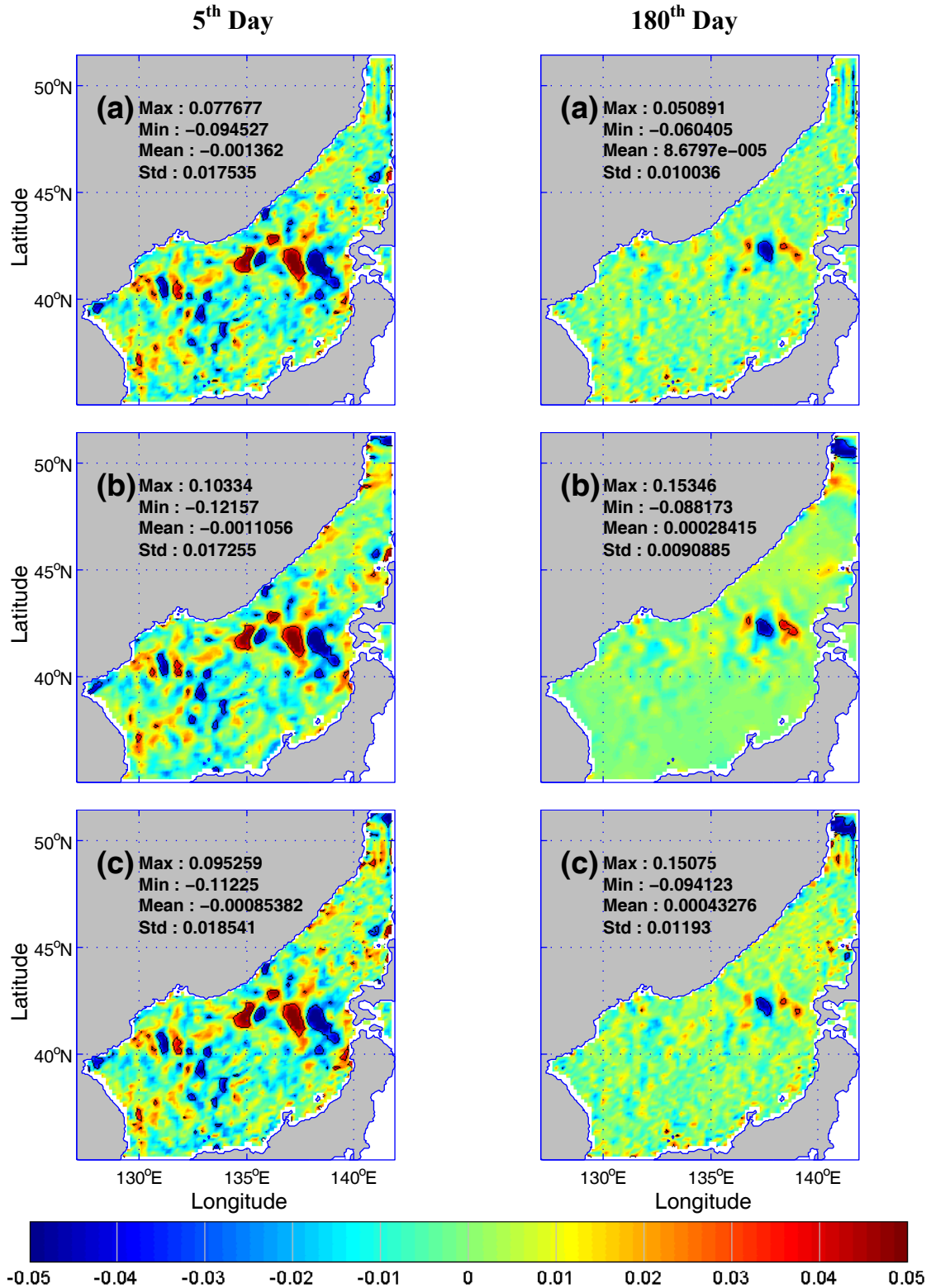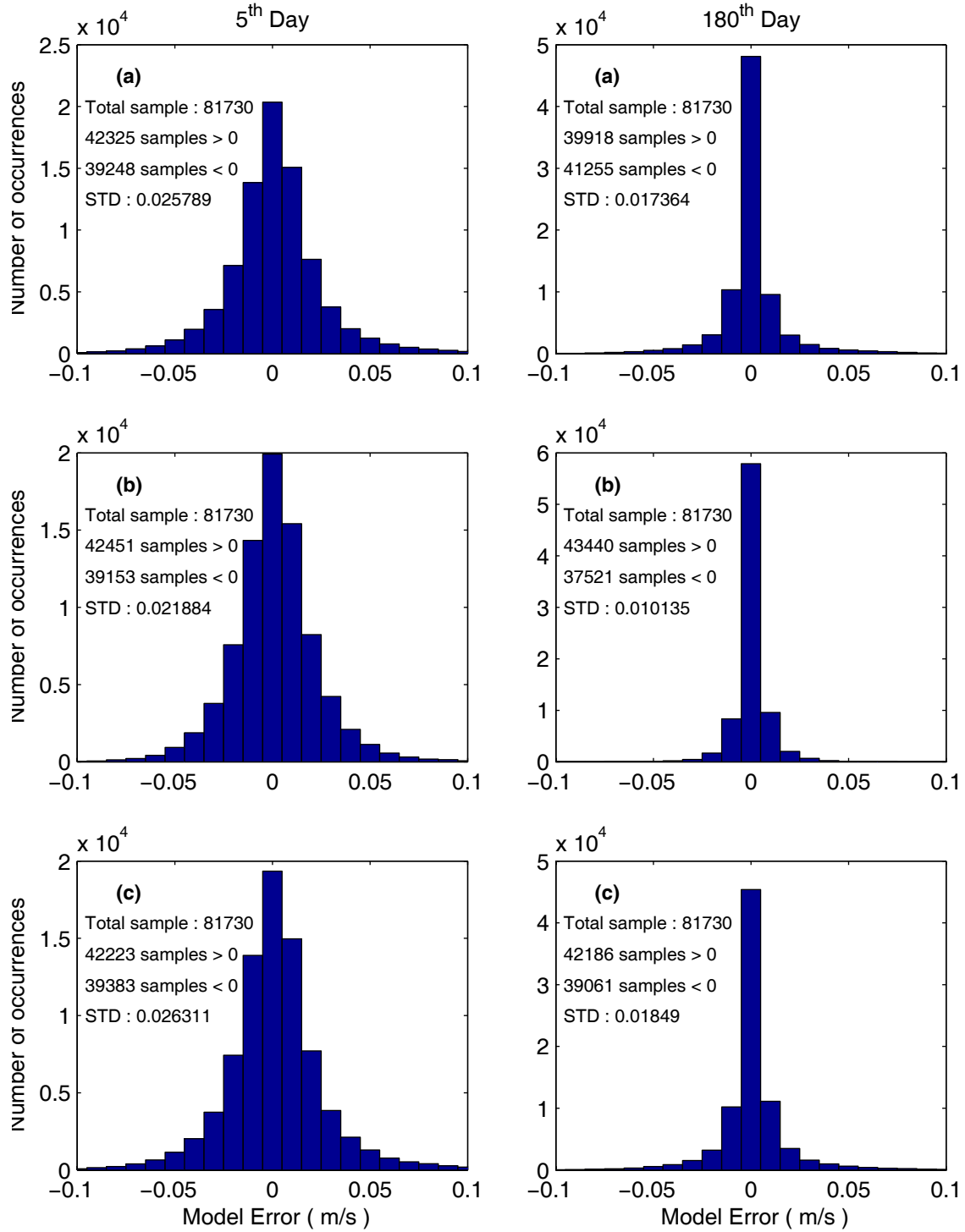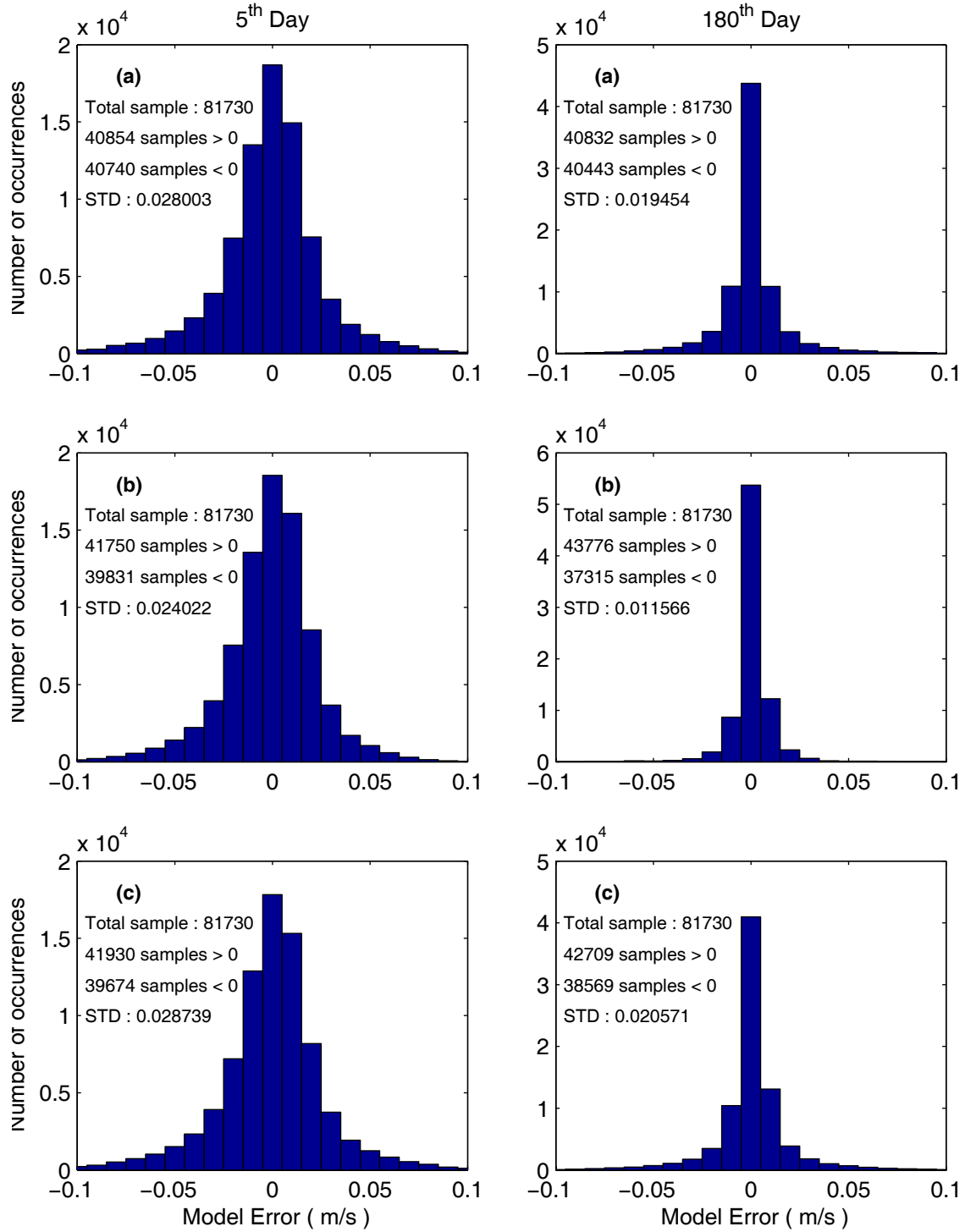
63

2.   The Root Mean Square Error (RMSE)

a.   *The Vertical Variation*

The Root Mean Square Error, calculated by equation (12), is used to evaluate the model performance. For the vertical profile of RMSE, two plots contained the errors caused by these three experimental runs for the horizontal velocity (**V**) fields made on both the 5th day (day-185) and the 180th day (day-360) after the day of model integration (day-180). These plots are shown in Figure 34.

As seen in this figure, the RMSE on the 5th day reveals that a higher value occurs above sigma level 8, which indicates that some stronger effects on model prediction occur at those levels. The maximum RMSE occurs in Run 11 at level 1 with a value of 0.08 m/s. These features are similar for the RMSE on the 180th day. The maximum RMSE occurs in Run 11 at level 1 with a value of 0.075 m/s. Although no obvious differences take place between Run 9 and 11, the RMSE caused by Run 11 has the largest value among these three experimental runs. In addition, these values of RMSE decrease with depth (rapidly above sigma level 8).

b.   *The Temporal Evolution*

The temporal evolution of vertically averaged RMSE for horizontal velocity (**V**) fields from the 5th day to the 180th day is shown in Figure 35. As seen in this figure, a significant difference exists among these three curves of RMSE for the horizontal velocity (**V**) fields (more RMSE is caused by Run 11). As observed, the RMSE is largely determined due to the initial uncertainty in the early period (before the 45th day), the lateral boundary transport uncertainty in the middle period (between the 45th day and the 155th day) and the uncertain winds in the late period (near the 180th day). The RMSE of horizontal velocity oscillates and generally decreases with time with a peak value on the 5th day of 0.035, 0.034 and 0.031 m/s in Run 11, 9 and 10, respectively. As in previous results, the higher RMSE is caused by Run 11 than by Run 9 and 10.

5th Day   **180th Day**

Figure 34.   RMSE of V in (a) Run 0 – Run 9, (b) Run 0 – Run 10 and (c) Run 0 – Run 11 on the 5th day and the 180th day after the model integration.

Figure 35.   Temporal evolution of vertically averaged RMSE of V in (a) Run 0 – Run 9, (b) Run 0 – Run 10 and (c) Run 0 – Run 11.

65

3.   The Relative Root Mean Square Error (RRMSE)

a.   The Vertical Variation

The Relative Root Mean Square Error, calculated by equation (13), is also commonly used for evaluating the model performance. For the vertical profile of RRMSE, two plots contained the errors caused by these three experimental runs for the horizontal velocity (**V**) fields made on both the 5th day (day-185) and the 180th day (day-360) after the day of model integration (day-180). These plots are shown in Figure 36.

As seen from this figure, the RRMSE on the 5th day reveals that the relatively higher RRMSE occurs in Run 11. The maximum RRMSE occurs in Run 11 at level 1 with a value of 0.73. For the RRMSE on the 180th day, it also reveals that the relatively higher RRMSE of all three fields occurs in Run 11. Except for Run 10, a higher value of RRMSE is present above sigma level 8, which indicates some stronger effects on model prediction occurring at those levels. The maximum RRMSE occurs in Run 11 with a value of 0.78 at level 1 for horizontal velocity. As in previous plots, although no obvious differences exist between Run 9 and 11, the RRMSE caused by Run 11 has a relatively higher value among these three experimental runs. Generally, the RRMSE decreases with depth (rapidly above sigma level 8) except for Run 10. As observed, the RRMSE of horizontal velocity in Run 11 is quite significant, especially above sigma level 8 (around 73 % and 78 % on the 5th day and the 180th day at the surface level, respectively).

b.   The Temporal Evolution

The temporal evolution of vertically averaging RRMSE for horizontal velocity (**V**) fields from the 5th day to the 180th day is shown in Figure 37. As seen in this figure, significant differences exist among these three curves of RRMSE for the horizontal velocity (**V**) fields (more RRMSE was caused by Run 11). As observed, the RRMSE is largely determined due to the initial uncertainty in the early period (before the 40th day), the lateral boundary transport uncertainty in the middle period (between the 40th day and the 160th day) and the uncertain winds in the late period (near the 180th day).

The RRMSE of horizontal velocity oscillates and generally decreases with time with a peak value on the 5th day of 0.52, 0.5 and 0.48 in Run 11, 9 and 10, respectively. As in all previous results, the higher RRMSE is caused by Run 11 than by the Run 9 and 10.
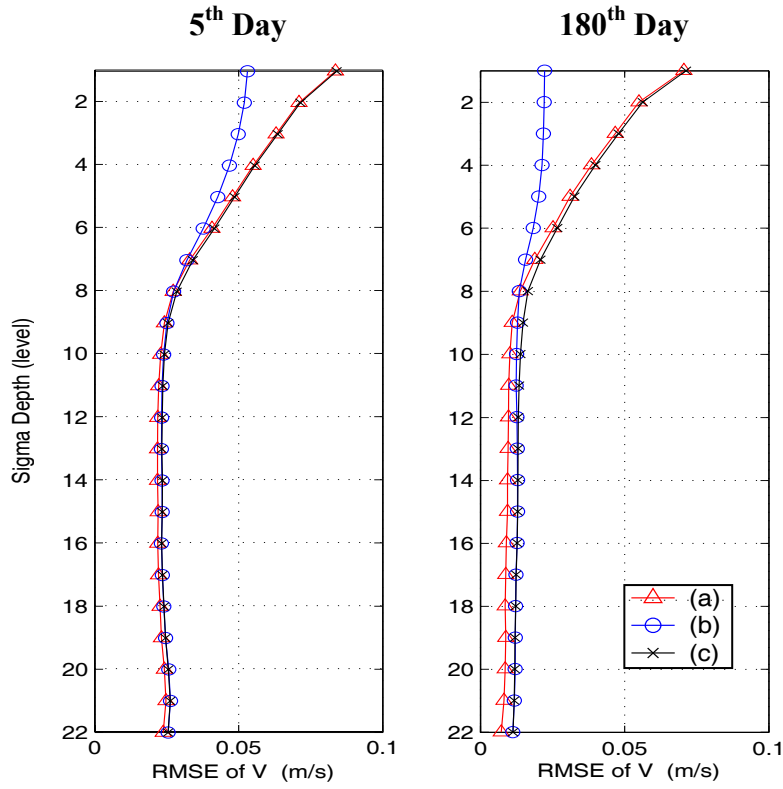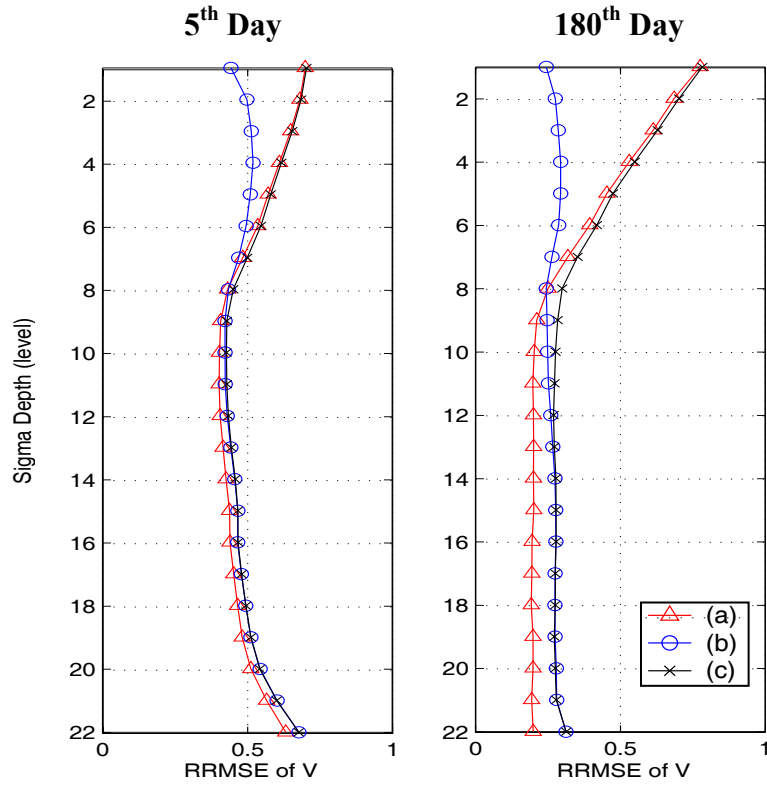
Figure 36.   RRMSE of V in (a) Run 0 – Run 9, (b) Run 0 – Run 10 and (c) Run 0 –
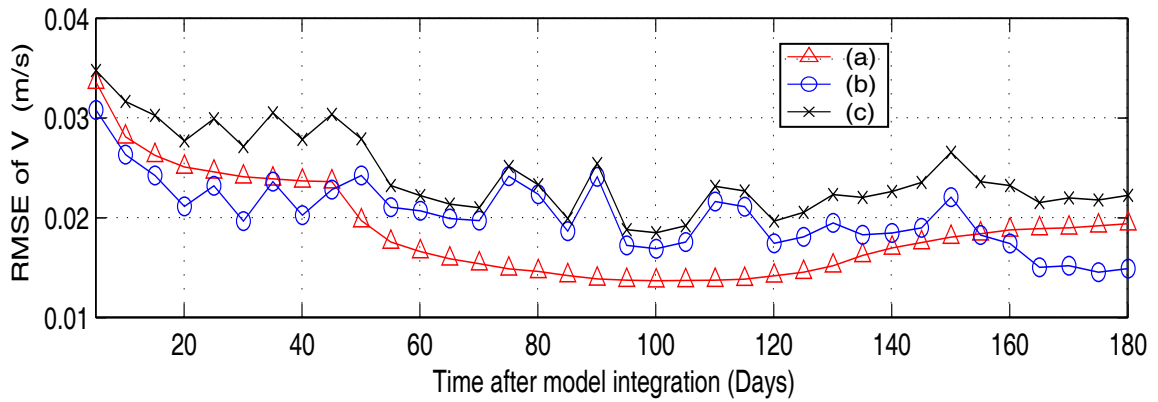Run 11 on the 5th day and the 180th day after the model integration.
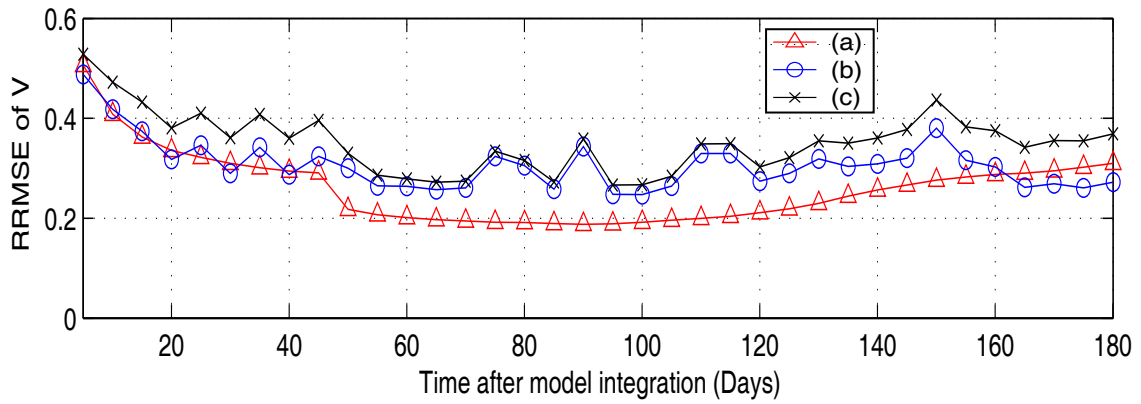
Figure 37.   Temporal evolution of vertically averaged RRMSE of V in (a) Run 0 –
Run 9, (b) Run 0 – Run 10 and (c) Run 0 – Run 11.

68

VII. CONCLUSIONS

In this thesis several experiments were conducted in order to investigate the model errors due to input uncertainty of the velocity initial conditions, wind forcing and lateral boundary transport. The RRMSE of the horizontal velocity field in these experiments is summarized in Table 7.

Experiment	Vertically averaged RRMSE		Max. RRMSE	
	Min.	Max.	5th Day	180th Day
For uncertain **velocity initial conditions**	20%	50%	**70%** near the surface	**25%** near the surface
For **0.5 m/s noise intensity**	8%	19%	**35%** near the surface	**50%** near the surface
For **1.0 m/s noise intensity**	11%	28%	**60%** near the surface	**80%** near the surface
For **noise intensity as 5%** of transport	9%	20%	**14%** near the bottom	**18%** near the bottom
For **noise intensity as 10%** of transport	17%	34%	**24%** near the bottom	**28%** near the bottom
For uncertain **initial condition** and **wind forcing**	20%	52%	**70%** near the surface	**77%** near the surface
For uncertain **initial condition** and **lateral boundary transport**	27%	50%	**65%** near the bottom	**35%** near the bottom
For uncertain **initial condition**, **wind forcing** and **lateral boundary transport**	30%	55%	**73%** near the surface	**78%** near the surface

Table 7   Summary of the RRMSE in each experiment.

For uncertain velocity initial conditions with and without diagnostic initialization, the model errors are quite comparable and significant, but they decrease with time. For diagnostic initialization, the magnitude of model errors is less dependent on the initialization period no matter if it is 30 days or 90 days. The vertically averaged RRMSE of the horizontal velocity decreases rapidly from 50% (the maximum value) on the 5th day to 20% (the minimum value) on the 50th day and then slightly oscillates with time near 20% to the 180th day. The RRMSE of horizontal velocity is 70% near the surface and 50% near the bottom on the 5th day and 25% near the surface and 20% near the bottom on the 180th day.

For uncertain wind forcing with the Gaussian random noise, the model error increases with time and noise intensity. The vertically averaged RRMSE of the horizontal velocity fluctuates with time. For the noise intensity of 0.5 m/s, it increases slowly from 11% on the 5th day to 12% on the 45th day and then decreases to 8% (the minimum value) on the 75th day and then increases again to 19% (the maximum value) on the 180th day. For the noise intensity of 1.0 m/s, it increases slowly from 18% on the 5th day to 20% on the 45th day and then decreases rapidly to 11% (the minimum value) on the 75th day and then increases again to 28% (the maximum value) on the 180th day. The maximum RRMSE of horizontal velocity, occurring near the surface, increases from 35% on the 5th day to 50% on the 180th day for noise intensity of 0.5 m/s, and increases from 60% on the 5th day to 80% on the 180th day for noise intensity of 1.0 m/s. The model errors generally decrease with depth and become small below sigma level-8.

For uncertain lateral boundary transport with the Gaussian random noise, the model error increases with time and noise intensity. The vertically averaged RRMSE of the horizontal velocity fluctuates with time between 9% and 20% (17% and 34%) for the noise intensity to be 5% (10%) of the transport of the control run. It generally increases with time from the 5th day to the 150th day with a peak value of 20% for 5% noise and 34% for 10% noise and then decreases with time to 15% for 5% noise and to 22% for 10% noise on the 180th day. The maximum RRMSE of horizontal velocity, occurring near the bottom, increases from 14% on the 5th day to 18% on the 180th day for 5% noise, and increases from 24% on the 5th day to 28% on the 180th day for 10% noise. The model errors generally increase with depth.

70

For combined uncertain initial condition (30 day period diagnostic initialization) and wind forcing (1.0 m/s noise intensity), the vertically averaged RRMSE of the horizontal velocity fluctuates between 52% and 20% while decreasing from 52% on the 5th day to 20% on the 50th day and then increasing slowly to 32% on the 180th day. The model uncertainty is largely determined due to the initial uncertainty in the early period (before the 50th day) and due to the uncertain winds in the late period (near the 180th day). The maximum RRMSE of horizontal velocity, occurring near the surface, increases from 70% on the 5th day to 77% on the 180th day.

For combined uncertain initial condition (30 day period diagnostic initialization) and lateral boundary transport (10% noise intensity), the vertically averaged RRMSE of the horizontal velocity fluctuates between 50% and 27% while decreasing from 50% on the 5th day to 30% on the 30th day and then oscillates between 27% and 38% with time to 29% on the 180th day. The model uncertainty is largely determined due to the initial uncertainty in the early period (before the 50th day) and the lateral boundary transport uncertainty in the late period (near the 150th day). The maximum RRMSE of horizontal velocity, occurring near the bottom, decreases from 65% on the 5th day to 35% on the 180th day.

For combined uncertain initial condition (30 day period diagnostic initialization), wind forcing (1.0 m/s noise intensity) and lateral boundary transport (10% noise intensity), the vertically averaged RRMSE of the horizontal velocity fluctuates between 55% and 30% while decreasing from 55% on the 5th day to 36% on the 30th day and then oscillates between 30% and 45% with time to 38% on the 180th day. The model uncertainty is largely determined due to the initial uncertainty in the early period (before the 50th day), the lateral boundary transport uncertainty in the middle period (between the 50th day and the 150th day) and the uncertain winds in the late period (near the 180th day). The maximum RRMSE of horizontal velocity, occurring near the surface, increases from 73% on the 5th day to 78% on the 180th day.

As the table demonstrates, the RRMSE with such higher values in each experiment reveal that the model uncertainty due to these input uncertainties (the velocity initial conditions, wind forcing and lateral boundary transport) is very significant.

Therefore, it is necessary to reduce these uncertainties to achieve better prediction of the ocean behavior. In addition, the results in this thesis can only be applied to this specific numerical ocean model (POM), study area (JES) and model setup (i.e., resolution). Applying these results to other ocean models, areas or model setups needs further investigation.

LIST OF REFERENCES

Bang, I., J-K Choi, L. Kantha, C. Horton, M. Cliford, M-S. Suk, K-I Chang, S.Y. Nam, and H-J Lie, "A hindcast experiment in the East Sea (Sea of Japan)", *La mer*, 34, 108-130, 1996.

Bennett, A., *Inverse methods in physical oceanography*, Cambrige University Press, 346, 1992.

Blumberg, A., and G. Mellor, "A description of a three dimensional coastal ocean circulation mode", edited by N.S. Heaps, *Three-Dimensional Coastal Ocean Models*, American Geophysics Union, Washington D.C., 1-16, 1987.

Chapman, D., "Numerical treatment of cross-shelf open boundaries in a barotropic ocean model", *J. Phys. Oceanogr.*, 15, 1060-1075, 1985.

Chu, P.C., "P-vector method for determining absolute velocity from hydrographic data", *Marine Tech. Soc. J.*, 29(3), 3-14, 1995.

Chu, P.C., C.W. Fan, and L.L. Ehret, "Determination of open boundary conditions with an optimization method", *J. Atmos. Ocea*. Tech., 1997.

Chu, P.C., Y.C. Chen, and S.H. Lu, "Temporal and spatial variabilities of Japan Sea surface temperature and atmospheric forcings", *J. Oceanogr.*, 54, 273-284, 1998.

Chu, P.C., Y. Chen, and S. Lu, "Japan/East Sea (JES) Subpolar Front meandering and eddy shedding in May 1995", *Proceedings of the CREAMS'99 International Symposium*, Fukuoka, Japan, p 11-13, Jan. 26-28, 1999a.

Chu, P.C., "Two kinds of predictability in the lorenz system", *J. Atmos. Sci.*, 1999b.

Chu, P.C., S.H. Lu, and W.T. Liu, "Uncertainty of south china sea prediction using NSCAT and national centers for environmental prediction winds during tropical storm Ernie, 1996", *J. Geophys. Res.*, 1999c.

Chu, P.C., J. Lan, and C.W. Fan, "Japan/East Sea (JES) seasonal circulation and thermohaline variabilities, Part 1, Climatology", *J. Phys. Oceanogr.*, 244-271, 2001a.

Chu, P.C., J. Lan, and C.W. Fan, "Japan/East Sea (JES) seasonal circulation and thermohaline variabilities, Part 2, A variational P-vector method", *J. Phys. Oceanogr.*, 2886-2902, 2001b.

Chu, P.C., and J. Lan, "Extremely strong thermohaline source/sinks generated by diagnostic initialization", *Geophysical Research Letters*, 30 (6), 2003.

Gong, Y., and C.G. Park, "On the oceanographical character of the low temperature region in the eastern sea of Korea", *Bull. Fish. Res. Dev. Agency*, Korea., 4, 69-91, 1969.

Hase, H., J.-H. Yoon, and W. Koterayama, "The Branching of the Tsushima Warm Current along the Japanese coast", *Proceedings of the CREAMS'99 International Symposium*, Fukuoka, Japan, pp. 19-22, Jan. 26-28, 1999.

Hogan, P.J., and H.E. Hurlburt, "Impact of upper ocean topographical coupling and isopycnal outcropping in Japan/East Sea models with 1/8 to 1/64 resolution", *J. Phys. Oceanogr.*, 30, 2535-2561, 2000a.

Hogan, P.J., and H.E. Hurlburt, "Modeled surface circulation in the Japan/East Sea: Impact of using different climatological wind forcing sets", *Proceedings of the International Conference on Coastal Ocean and Semi-Enclosed Seas: Circulation and Ecology Modeling and Monitoring*, Moscow, Russia, 57-60, 2000b.

Holloway, G.T. Sou, and M. Eby, "Dynamics of circulation of the Japan Sea", *J. Mar. Res.*, 53, 539-569, 1995.

Isoda, Y., and S. Saitoh, "The northward intruding eddy along the east coast of Korea", *J. Oceanogr.*, 17, 265-276,1993.

Isoda, Y., S. Saitoh, and M. Mihara, "SST structure of the Polar Front in the Japan Sea", *Oceanography of Asian Marginal Seas*, ed. by K. Yakano, Elsevire. 103-112, 1991.

Kawabe, M., "Branching of the Tsushima Current in the Japan Sea, Part I: Data analysis", *J. Oceanogr. Soc.*, 38, 95-107, 1982a.

Kawabe, M., "Branching of the Tsushima Current in the Japan Sea, Part II: Numerical experiment", *J. Oceanogr. Soc.*, 38, 183-192, 1982b.

Kim. C.-H., and J.-H. Yoon, "Modeling of the wind-driven circulation in the Japan Sea using a reduced gravity model", *J. Oceanogr.*, 52, 359-373, 1996.

Kim, K., and J.Y. Chung, "On the salinity-minimum layer and dissolved oxygen-maximum layer in the East Sea (Japan Sea)", *Ocean Hydrodynamics of the Japan and East China Sea*, ed. by T. Ichiye, Elsevier, Amsterdam., 55-65, 1984.

Kim, Y.G., and K.K. Kim, "Intermediate Waters in the East/Japan Sea", *Journal of Oceanography*, 55, 123-231, 1999.

Levitus, S., "Climatological atlas of the World Ocean", NOAA Prof. Paper 13, Washington D.C., 1982.

Lorenz, E.N., "Deterministic nonperiodic flow", *J. Atmos. Sci.*, 20, 130-141, 1963.

Maizuru Mar. Observ., *Bulletin of the Maizuru Marine Observatory*, 1997.

Martin, S., and M. Kawase, "The southern flux of sea ice in the Tatarskiy Strait, Japan Sea and the generation of the Liman Current", *J. Marine Res.*, 56, 141-155, 1998.

Miyazaki, M., "On the water masses of the Japan Sea", *Bull. Hokkaido Reg. Fisher. Res. Lab.*, 7, 1-65 (in Japanese with English abstract), 1953.

Moriyasu, S., "The Tsushima Current", ed. by H. Stommel and K. Yoshida, *Kuroshio-Its Physical Aspects*, Univ. of Tokyo Press, Tokyo., 353-369, 1972.

Oliger, J., and A. Sundstrom, "Theoretical and practical aspects of some initial boundary value problems in fluid dynamics", *SIAM J. Appl. Math.*, 35(3), 419-446, 1978.

Orlanski, I., "A simple boundary condition for unbounded hyperbolic flows", *J. Comput. Phys.*, 21, 251-269, 1976.

Preller, R.H., and P.J. Hogan, "Oceanography of the Sea of Okhotsk and the Japan/East Seas", *In The Sea*, ed. by A.R. Robinson and K.K. Brink, John Wiley and Sons, Inc., 11, 429-481, 1998.

Seiler, U., "Estimation of the open boundary conditions with the adjoint method", *J. Geophys. Res.*, 98(C12), 22855-22870, 1993.

Senjyu, T., "The Japan Sea Intermediate Water: its characteristics and circulation", *J. Oceanogr.*, 55, 111-122, 1999.

Seung, Y.H., and K. Kim, "On the possible role of local thermal forcing on the Japan Sea circulation", *J. Oceanol. Soc.*, Korea, 24: 1-14, 1989.

Seung, Y.H., and S.Y. Nam, "A numerical study on the barotropic transport of the Tsushima Warm Current", *La mer*, 30, 139-147, 1992.

Shin, H.-R., S.-K. Byun, and C. Kim, "The characteristics of structure of warm eddy observed to the northwest of Ulleungdo in 1992", *J. Oceanol. Soc.*, Korea, 30, 39-56 (in Korean with English abstract), 1995.

Shin, C.W., S.K. Byun, and C.S. Kim, "Comparison between Geostrophic Currents in the southwestern Part of the East Sea", *J. Oceanol. Soc.*, Korea, 31, 89-96, 1996.

Shulman, I., and J.K. Lewis, "Optimization approach to the treatment of open boundary conditions", *J. Phys. Oceanogr.*, 25, 1006-1011, 1995.

Smagorinsky, J., "General circulation experiments with the primitive equations, I. The basic experiment", *Mon. Weather Rev.*, 91, 99-164, 1963.

Toba, Y., K. Tomizawa, Y. Kurasawa, and K. Hanawa, "Seasonal and year-to-year variability of the Tsushima-Tsugaru Warm Current system with its possible cause", *La Mer.*, 20, 41-51, 1982.

Tomczak, M., and J.S. Godfrey, *Regional Oceanography: an Introduction*, 1st ed., Pergamon, 1994.

Uda, M., "The results of simultaneous oceanographic investigations in the Japan Sea and its adjacent waters in May and June", *J. Imp. Fish. Exp. Sta.*, 5, 57-190 (in Japanese), 1934.

Yi, S.U., "Seasonal and secular variations of the water volume transport across the Korea Strait", *J. Oceanogr. Soc.*, Korea., 1, 7-13, 1966.

Yoon, J.-H., "Numerical experiment on the circulation in the Japan Sea, Part I. Formation of the East Korean Warm Current", *J. Oceanogr. Soc.*, Japan, 38, 43-51, 1982a.

Yoon, J.-H., "Numerical experiment on the circulation in the Japan Sea Part, III. Mechanism of the Nearshore Branch of the Tsushima Current", *J. Oceanogr. Soc.*, Japan, 38, 125-130, 1982b.

THIS PAGE INTENTIONALLY LEFT BLANK

INITIAL DISTRIBUTION LIST

1.   Defense Technical Information Center
        Ft. Belvoir, Virginia

2.   Dudley Knox Library
        Naval Postgraduate School
        Monterey, California

3.   Chairman Code OC
        Department of Oceanography
        Naval Postgraduate School
        Monterey, California

4.   Professor Peter C. Chu Code OC/CU
        Department of Oceanography
        Naval Postgraduate School
        Monterey, California

5.   Mr. Steve D. Haeger
        Naval Oceanographic Office
        Stennis Space Center, Mississippi

6.   LCDR. Chin-Lung Fang
        The Headquarter of the 168th Fleet
        Taiwan, Republic of China Navy